

MASTER's Degree in BIOMEDICAL ENGINEERING



**Politecnico
di Torino**

MASTER's Degree Thesis

**Novel technique for Pulse Wave
Detection: Electrical Bio-Impedance
Plethysmography**

Supervisors

Prof. DANILO DEMARCHI

Ph.D. IRENE BURAIOLI

Ph.D. ALESSANDRO SANGINARIO

Candidate

SANTIAGO CARO ZAPATA

DECEMBER 2023

Abstract

Cardiovascular diseases (CVDs) are the leading cause of death worldwide, taking more than 17 million lives according to the World Health Organization (WHO) and costing approximately €210 billion annually to the European Union. Each disease has its risk factors, and one of the most common denominators is the development of atherosclerosis, which is characterized by the thickening or stiffening of the arteries.

Arterial stiffness is due to the loss of the artery walls' distensibility, causing increased blood pressure and speed with which the pulse wave propagates in the arterial tree. Relative to the latter, the Pulse Wave Velocity (PWV) measurement has demonstrated to be one of the best non-intrusive ways to estimate arterial stiffening.

Currently, the most reliable methods to measure the PWV, are based Pulse Wave (PW) acquisition at two points using tonometers, usually the carotid and femoral arteries, computing the velocity between them. These devices are operator-dependent because of their functional principle: the sensor must be held above the artery with adequate pressure during the entire PW recording time, which makes the signal very susceptible to management. Therefore, nowadays, PWV acquisition techniques present several limits for developing wearable devices for continuous monitoring.

As the first step to measure the PWV is to acquire the PW, this thesis project proposes an innovative sensing technology for the PW measurement that would not require expert operators and even be a wearable device. Impedance plethysmography (IPG) was considered because it relates the changes in impedance to blood volume in the artery. For this purpose, the scope of this thesis is to design and implement a system to acquire the PW measuring the IPG.

In this project, the evaluation board eval-ADuCM355 from Analog Devices was used, designed explicitly for impedance measurements, has been selected. The board injects a fixed alternating voltage between two electrodes and uses the Discrete Fourier Transform (DFT) to calculate the impedance of the zone of interest. Three ways to use the microcontroller were tested. The first method estimated the impedance using its internal components and signal processing; the second one used the ADuCM355 to inject the fixed voltage while the acquisition and calculations were performed externally; the last one used the internal components to inject and

acquire the signal, but the impedance estimation was done in post-processing after the signal was sent via Serial Peripheral Interface (SPI).

The third method was the most promising to evaluate the impedance. Therefore, different acquisition sites, electrode placements, and system settings were tested, seeking to find the most suitable configuration to acquire the pulse wave. The parameters evaluated in each configuration were the inter-electrode distance, the relative angle between electrodes and the artery, and the amplitude of the excitation voltage.

Finally, with the selected configurations, it was possible to acquire the pulse wave signal, which, in later studies, may be helpful to develop a wearable device for PW detection and PWV monitoring.

Acknowledgements

It is incredible how two years have gone by so fast and too slow at the same time. Two years full of changes, challenges and emotions, that taught me a lot and make me grow academically and personally.

First, I would like to thank the eLions group, which allowed me work with them on this project, giving me all the support and the tools to develop it. Also, I am thankful with the Professor Danilo Dermachi, Ph.D. Irene Buraioli and Ph.D. Alessandro Sanginario for giving me this opportunity and being a great support during all the process. Thanks to the PhD student Marco Pogliano, who was available to advise me and share his knowledge since the first moment.

In second place, I thank my friends Jesica, Ilaria, Daniela, Karen and Manuela for being willing to help and encourage me even when I could not see the end of the road. To my Turin family, Jose, Laura, Maria José, Carolina, Andrea, and all my Colombian and Italian friends who made these two years more wonderful than I expected. Also, to my friends in Colombia who, regardless of distance, supported me and looked forward to my process.

Finally and most important, I thank my family, especially my father, mother, brother and grandmothers, who believed in me and supported me not just from the moment I had this crazy idea to come to Italy but also in every step of my life.

Table of Contents

List of Tables	VIII
List of Figures	IX
Acronyms	XIV
1 Introduction	1
2 Background	3
2.1 Cardiovascular anatomy and physiology	3
2.1.1 Heart	4
2.1.2 Blood vessels	10
2.1.3 Blood	12
2.2 Cardiovascular diseases and arterial stiffness	13
2.3 Pulse Wave Velocity	14
2.3.1 Pulse Wave	15
2.4 PWV estimation	16
2.4.1 Clinical devices	18
2.5 Plethysmography signal	21
2.5.1 Impedance Plethysmography (IPG)	21
3 Materials	24
3.1 ADuCM355	24
3.1.1 Impedance measurement system	25

3.1.2	Communication protocols	27
3.2	Raspberry	29
3.3	NiDAQ	29
3.4	g.HIAMP	30
4	Methods	32
4.1	First method: Internal sampling and processing of ADuCM355's . .	33
4.2	Second method: NiDAQ sampling and external processing	35
4.3	Third method: SPI transmission to Raspberry and external processing.	37
4.4	Validation Tests	39
4.5	In vivo test: IPG signal acquisition	40
5	Results	42
5.1	Resistors measurement	42
5.2	Potentiometer test	44
5.3	Respiration test	48
5.4	Plethysmography acquisition test	50
6	Conclusions	57
	Bibliography	59

List of Tables

4.1	Influence of DFT's number of samples on the sampling frequency for the original and modified method.	35
-----	---	----

List of Figures

2.1	Cardiovascular circuitry indicating the cardiac output percentage to each organ in a resting subject [6].	4
2.2	Heart layers. The innermost layer is the endocardium, and the outer layer is the pericardium, which includes the epicardium, pericardial cavity, parietal layer of the serous pericardium, and the fibrous pericardium.	5
2.3	Heart anatomy, composed of ventricles, atria, cardiac valves and the great vessels.	6
2.4	Left heart cardiac cycle, showing the atrial, ventricular and aortic pressures. Left ventricular volume, electrocardiogram (ECG) and phonocardiogram [10].	7
2.5	Electrocardiogram (ECG). Shows the polarization (P and QRS complex) and repolarization (T) waves [10].	8
2.6	ECG leads configurations: a) Augmented unipolar limb leads the three bipolar limb leads, b) There is the augmented unipolar limb leads overlapped with the first configuration, c) Position of electrodes for the precordial leads [11].	9
2.7	Blood vessels and the blood course throughout them starting in the arteries, arterioles, capillaries, venules and finally veins.	10
2.8	Artery structure and development of the atherosclerosis [10].	14
2.9	Typical pulse waveform in aortic arch.	15
2.10	a) Collecting sites for the arterial pulse [19], b) Morphological and temporal differences between the PW in the carotid and femoral artery.	16
2.11	PW acquired in carotid and femoral arteries; and PTT assessment with ECG as reference.	17

2.12	Imaging techniques for PWV measurement. a) MRI at the aortic arch [22]; b) US at femoral artery synchronized with ECG [23]. . . .	19
2.13	Tonometry sensor [20].	19
2.14	<i>Arteriograph</i> [®] device. Use of one acquisition cite for PWV measurement [25].	20
2.15	Impedance model of the blood and its surrounding tissue	22
2.16	a) Electrodes placement for IPG acquisition. Outter electrodes inject current and inner electrodes measure the voltaje; b)IPG signal with its AC (blue), DC (Z_0 offset) and the pulsatile (red) components [5].	22
3.1	EVAL-ADuCM355QSPZ evaluation board	25
3.2	Simplified system for impedance measurement of the ADuCM355. Highlighted in blue dashed line is the Waveform generation macro-block, in red the voltage injection, green the current measurement, and magenta the post processing.	26
3.3	ADuCM355 connection to a external device for SPI communication	27
3.4	SPI communication protocol	28
3.5	ADuCM355 connection to a external device for UART communication.	28
3.6	Raspberry pi 3 Model B	29
3.7	NiDAQ USB-6259	30
3.8	g.HIAMP for ECG and EEG acquisition	31
4.1	Flowchart of the first method . On the left is the original procedure and on the right is the process modified with the major change highlighted in red. On the middle is the sub-process to calculate the DFT's magnitude.	34
4.2	ADuCM355's impedance measurement system with external R_{TIA} . The voltage in that resistor is acquired with NiDAQ USB-6259 and processed in Matlab.	36
4.3	ADuCM355, Raspberry and computer connection for the third impedance measurement method.	37
4.4	On the left Raspberry's pipeline and on the right the ADuCM355's pipeline. The blue line represents the UART communication. While red and green lines, stands for SPI communication. Red for the CS signal and the green line for MOSI signal	38

4.5	Respiration test configuration, two electrodes connected to the ADuCM355 placed on the sides of the trunk.	40
4.6	IPG acquisition setup. a) All the systems connected to the subject. The g.HIAMP is enclosed in red, the ECG electrodes are enclosed in blue, the ADuCM355 in yellow and the IPG electrodes in green. b) Parallel configuration of IPG electrodes. c) Perpendicular configuration of IPG electrodes	41
5.1	Results for resistors measurement for first method. It is compared the real resistor value with the measured.	43
5.2	Second method results for resistors measurement. a) DFT's magnitude behavior, b) Comparison between real and measured resistance.	43
5.3	Third method results for resistors measurement. a) DFT's magnitude behavior, b) Comparison between real and measured resistance.	44
5.4	First method result for potentiometer test.	45
5.5	Signal recorded with the third method for the potentiometer test.	45
5.6	DFT spectrums for a) correct measurements and b)undesirable measures.	46
5.7	Acquired signal in time-domain before processing. Highlighted in the red box the lack of a data	47
5.8	Third method signal for potentiometer test after peak removal and interpolation processing.	48
5.9	Respiration signal acquired wiht the internal ADuCM355 processing method.	49
5.10	Third method signal for potentiometer test after peak removal and interpolation processing.	49
5.11	Third method signal for potentiometer test after peak removal and interpolation processing.	50
5.12	a)ECG signal, b)Impedance signal acquired with first measurement method c)Welch periodogram for the impedance signal.	51
5.13	Filtered impedance signal(Red) compared with ECG signal (blue).	52
5.14	a)ECG signal, b)Impedance signal acquired with electrodes perpendicular to the carotid axis placed 4cm between them, using the first measurement method, c) Welch periodogram for the impedance signal	53

5.15	Filtered signal acquired in perpendicular-4 cm electrodes configuration (red), compared with the ECG (blue).	53
5.16	a) ECG signal , b) Impedance signal (red) acquired with third measurement method, c) Welch periodogram for the impedance signal	54
5.17	Filtered signal acquired in perpendicular-4 cm electrodes configuration (red), compared with the ECG (blue).	54

Acronyms

CVD

Cardiovascular disease

WHO

World Health Organization

ESC

European Society of Cardiology

CVS

Cardiovascular system

PWV

Pulse Wave Velocity

PW

Pulse Wave

IPG

Impedance Plethysmography

DFT

Discrete Fourier Transform

SPI

Serial Peripheral Interface

ECG

Electrocardiogram

AV

Atrioventricular

SA

Sinoatrial

EU

European Union

PTT

Pulse Transit Time

MRI

Magnetic Resonance Imaging

US

Ultrasound

PPG

Photoplethysmography

AC

Alternating Current

DC

Direct Current

ADC

Analog-to-Digital converter

DAC

Digital-to-Analog converter

WG

Waveform Generator

LPF

Low-Pass Filter

TIA

Trans Impedance Amplifier

UART

Universal Asynchronous Receiver/Transmitter

PGA

Programmable Gain Amplifier

EAB

Excitation Amplifier Buffer

IDE

Integrated Development Environment

LAN

Local Area Network

MOSI

Master Out Slave In

MISO

Mater In Slave Out

CLK

serial Clock

CS

Chip Select

FIFO

Firs Input First Output

Chapter 1

Introduction

Cardiovascular diseases (CVDs) are the term used to refer to heart and blood vessel disorders, representing almost a third of the diseases worldwide in 2019, according to the World Health Organization (WHO). In the European Union (EU), there are more than 6 million new CVDs cases and 1.8 million deaths each year, costing over €210 billion in accordance with the European Society of Cardiology (ESC). The myocardial infarction and the stroke are the most common causes of death among the CVDs.

Many possible risk factors lead to suffering a heart attack or stroke, such as hypertension and atherosclerosis, which are among the most frequent [1]. These risk factors have in common that they are strongly correlated with arterial stiffness, which means it can be used as a predictor for the CVDs and for organ damage prevention [2].

The arterial stiffness describes the distensibility decrement of the artery walls and the capacity reduction of the vessels to store blood. In addition, due to the rigidity of the arteries, the Pulse Wave (PW) travels faster along the arterial tree, and its speed can be measured using the Pulse Wave Velocity (PWV), which is also used as an indirect measurement of the arteries' distensibility [3].

The PWV is the most reliable biomarker to assess arterial stiffness. The gold standard method to estimate it measures the time the PW takes to go from one artery to another, computing the velocity taking into account the Euclidean distance between the arteries, so the PW must be acquired in two of the main arteries, usually the carotid and the femoral [4].

Currently, the clinical devices for the PWV measurement use tonometric sensors, which must be held by an operator over the artery site that acquires the PW signal according to the pressure variation. Despite this being the most reliable method,

it requires a trained operator to avoid damage to the signal because of excessive pressure or changes in the angle between the sensor and the artery. In addition, this measuring principle is not suitable for continuous monitoring of PWV [4].

Changing the PW measurement principle is the propose to solve the enunciated problems, but remaining with the same technique to compute PWV. Impedance plethysmography (IPG) was the chosen physical principle because it can relate the change in impedance with the volume variation in the arteries. Therefore, this thesis project aims to design and implement a system for PW detection, measuring the electrical Bio-Impedance plethysmography signal.

Usually, the IPG signals are acquired using an array of four electrodes, injecting a fixed current between the external electrodes; the inner electrodes measure the voltage, and the impedance is computed using Ohm's relation [5]. However, in this project, the microcontroller ADuCM355 from Analog DevicesTM that was designed with an internal impedance measurement system, is used. The system only requires two electrodes and, contrary to the other methods, injects a fixed voltage, and the current is measured. The Discrete Fourier Transform (DFT) is used to demodulate the signal and calculate the impedance.

Initially, the ADuCM355 was used as the manufacturer suggested. However its sampling frequency was too low to identify a PW correctly; for this reason the microcontroller was tested in other two modalities in order to increase the sampling rate. The first involved an external acquisition with the NiDAQ USB-6259 and external signal processing in MATLAB®. In the second, the signal was acquired with the ADuCM355, and the data was transmitted via Serial Peripheral Interface (SPI) to a Raspberry Pi to process the signal on an external computer finally.

Different validation and a in-vivo tests were designed to assess each measurement methodology. Although the validation tests obtained adequate results, acquiring the PW signal in most in-vivo tests where different electrode placements and configurations were evaluated was impossible. Just using the original ADuCM355 methodology and putting the electrodes perpendicular to the axis of the carotid artery was possible to acquire a wave that lets think the IPG usage for the PW acquisition is feasible. However, the system and the signal processing require some improvements, and for the electrode placement, the number of tests must be increased to determine the most suitable locations and configurations.

Chapter 2

Background

2.1 Cardiovascular anatomy and physiology

The human body must guarantee the conditions for life, so it has to manage internally its temperature, oxygen concentration, pH level, and other vital variables. This property is referred to as homeostasis and it's controlled by the cardiovascular system (CVS) which has evolved into a complex network composed of a pump and a set of channels to transport materials such as nutrients and oxygen to the organs and to extract waste and carbon dioxide (CO_2) from them [6].

The exchange of chemical materials takes place between three types of watery compartments, the intracellular, interstitial, and plasma compartments. The plasma is pumped throughout the body to all the organs as seen in **Figure 2.1**. In this way when it passes through each one of them, the plasma draw from or release into the interstitial compartment the different products thanks to the network of capillaries that offer minimal resistance to the exchange of substances. At the same time, there is another exchange process between the interstitial and intracellular environments for the nutrients, metabolites, hormones and oxygen can reach the cells[6, 7].

To ensure the exchange of substances between the plasma and cells, a short distance between them, an adequate blood flow, and a correct chemical composition of the incoming (arterial) blood are necessary. Thus, the CVS has two circuits arranged in series, the *pulmonary circulation* composed of the right part of the heart and the lungs, where the blood is oxygenated and the CO_2 is eliminated (see figure **Figure 2.1**); and the *systemic circulation* structured of the left hearth and all systemic organs (except lungs) which are arranged in parallel. This allows to transport oxygenated blood of identical composition to each organ, but not

necessarily in the same amount, because this arrangement permits control of blood flow in response to the organs needs [6].

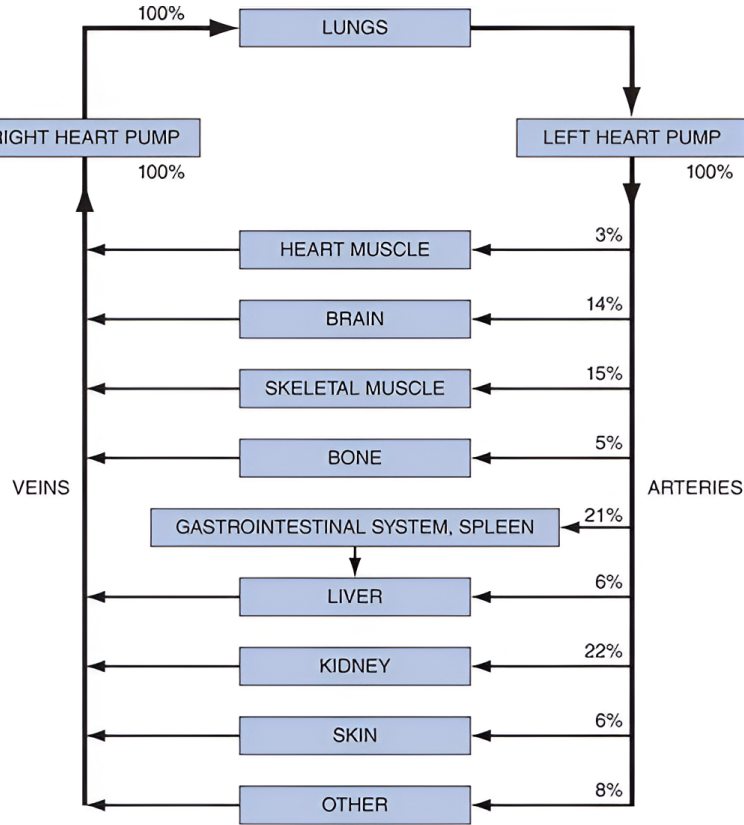


Figure 2.1: Cardiovascular circuitry indicating the cardiac output percentage to each organ in a resting subject [6].

As noted above, one of the main CVS's components is the heart, the organ in charge of pumping the blood throughout the body. However, other components are equally important, such as blood vessels (arteries, veins and capillaries) and the blood.

2.1.1 Heart

The heart has a shape similar to a cone and it is located between the lungs and behind the sternum in a place referred as mediastinum, slightly to the left of the midline of the chest. It is enclosed by a fibroserous sac called the pericardium, that protects and allows the heart to beat in a minimal friction environment. Its layer attached to the heart is the visceral pericardium also called epicardium. Internal to it is the myocardium which is the thickest layer and consists essentially of muscle

cells. Finally, the innermost layer is the endocardium and acts as a barrier between the heart and the blood [8]. In **Figure 2.2** the layers of the heart can be seen.

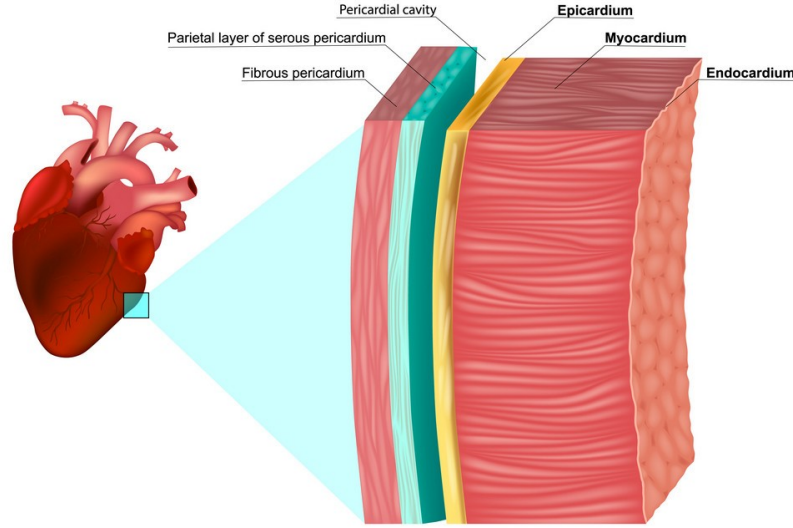


Figure 2.2: Heart layers. The innermost layer is the endocardium, and the outer layer is the pericardium, which includes the epicardium, pericardial cavity, parietal layer of the serous pericardium, and the fibrous pericardium.

The heart (see **Figure 2.3**) is composed of four muscular chambers. The two superior ones work as reservoirs for the blood returning to it and are called atria. The ventricles are the inferior chambers and are responsible for propelling blood outside the heart[9]. Fulfilling the function of barrier between the chambers are the septum, which divide the heart in two halves; and the cardiac valves between the atria and ventricles (atrioventricular valves), known as the tricuspid and mitral valves. Additionally, there are the pulmonary and aortic valves (semilunar valves) between the ventricles and great vessels. The four valves are designed to allow flow in just one direction and prevent backward leakage. They work passively, opening and closing themselves in response to the changes in the pressure difference between both sides of the valve [6, 8].

The change in the pressure inside the heart depends on what phase it is in while pumping blood to the whole body. Blood pumping is a cyclic process involving atria, ventricles and valves and is known as cardiac cycle.

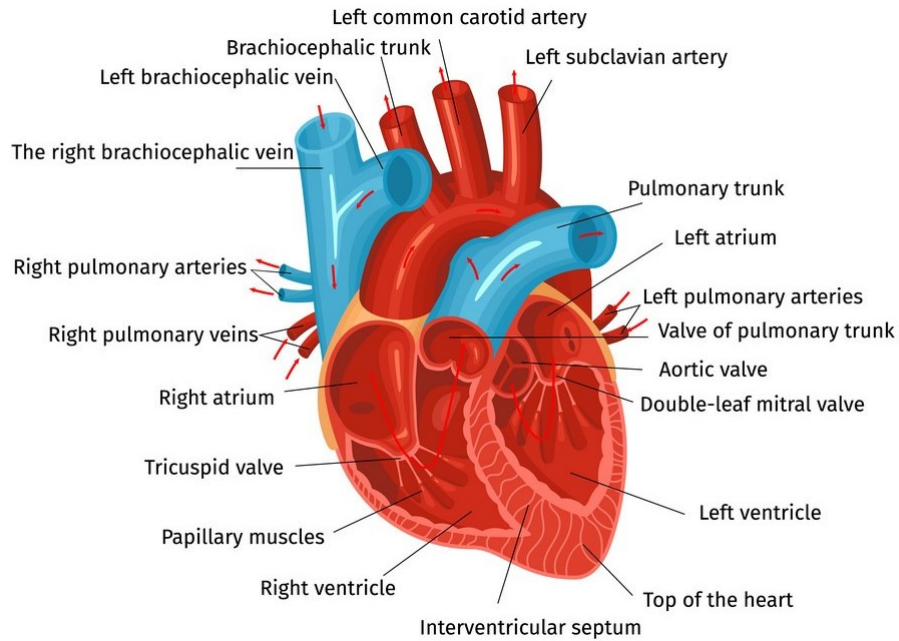


Figure 2.3: Heart anatomy, composed of ventricles, atria, cardiac valves and the great vessels.

Cardiac cycle

The cardiac cycle is a set of timed mechanical and electrical events that describe the processes that occurs between one heart beat and the next one. This cycle includes two major phases, systole and diastole. The first one occurs when the heart contraction happens and the second one is a period of relaxation. However, the cardiac cycle is not just two phases, within each one of them there are other subphases which explain the mechanical process done by every heart component [8, 10].

The complete cardiac cycle for the left heart, as shown in **Figure 2.4** , starts with the atrial systole, which is synchronized with the last part of the ventricular diastole. At that moment, the atrioventricular (AV) valves are open, the semilunar valves are closed, and the ventricle has about 80 % of the blood volume capacity. Then, atrial contraction drives additional blood that fills the ventricles and ends the diastole phase [7, 10].

Subsequently, the closure of the AV valves and ventricular contraction initiates the ventricular systole, thus sharply increasing the pressure until it is possible to open the pulmonary and aortic valves. That period is known as isovolumic

contraction. The contraction continues, the blood ejection starts and the ventricles empty quickly up to the pressure reaches its maximum and then slowly as the pressure decreases, getting to the point where semilunar valves close [10].

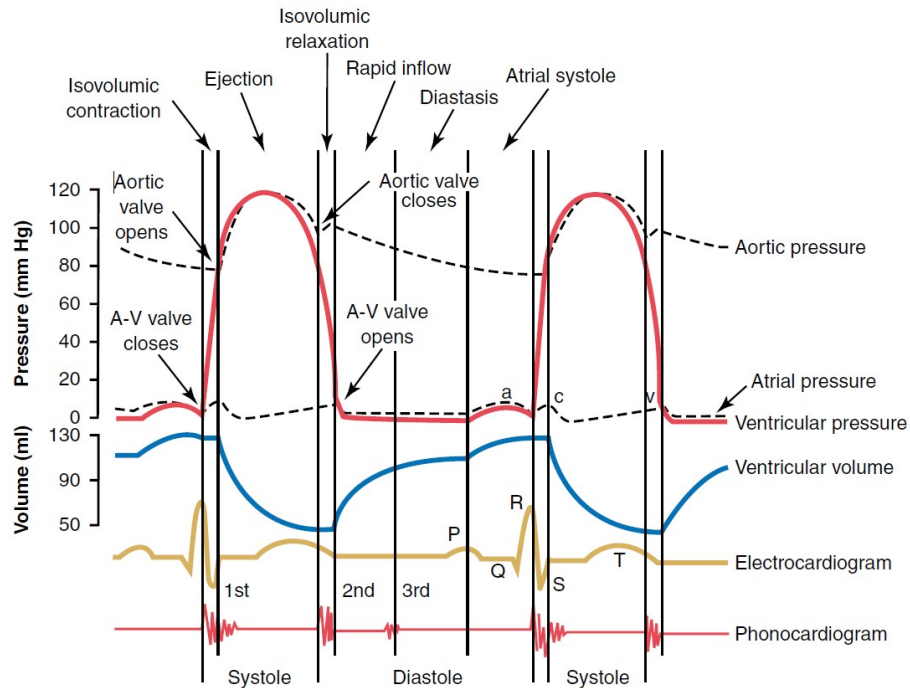


Figure 2.4: Left heart cardiac cycle, showing the atrial, ventricular and aortic pressures. Left ventricular volume, electrocardiogram (ECG) and phonocardiogram [10].

At that point, the systole finishes, and the diastole begins again. Initially, with isovolumic relaxation, the ventricle concludes the contraction, allowing the pressure to decrease steadily. The AV valves are opened when the pressure in the ventricles is lower than in the atria. This allows the ventricles to fill in three subphases: rapid inflow, diastasis, and atrial systole again to restart the cardiac cycle [7].

Most of these mechanical processes do not occur passively, an electrical excitation is required to activate the cardiac muscles, and additionally, it should be done rhythmically.

Electrical heart activity and Electrocardiogram (ECG)

A specialized excitatory and conductive system manages the electrical activity in the heart. This system's primary element is the sinus node or sinoatrial node (SA).

This node is located between the superior vena cava and the right atrium, in the wall of the last one. Other components like the AV node, AV bundle, and the inter-nodal pathways play an essential role, but the SA node is the one in charge of periodically activating the heart. For that reason, the SA node is known as the heart pacemaker because it exhibits an intrinsic rhythmical excitation. However, the other components could be able to do it, though the SA node emits the impulse faster than they do, avoiding their intrinsic excitation and in this way controlling the heartbeat [7, 10].

As described previously, the excitation begins, as the cardiac cycle does, at the SA node with the atria depolarization; then, with a little delay, the AV node is stimulated, and the cardiac impulse arrives at the ventricles and depolarizes them. The ventricular depolarization starts at the left part of the ventricular septum and continues to the right part; next, it goes to the heart apex, to return, at that time, through the walls to the AV junction to finally goes from the endocardium surface to the epicardium [7].

All those depolarization and re-polarization sequences cause electrical currents to spread around the adjacent tissues, which perceive these fluctuations, such as the algebraic sum of all action potentials. The recording of these signals is the ECG [10].

The ECG is composed of the P wave (see **Figure 2.5**) that describes the atrial depolarization before the atrial contraction begins; the depolarization also generates the QRS complex, but in this case, it is due to the ventricles, which do so prior to their contraction. Ultimately, the T wave is caused by the ventricles' re-polarization, which occurs while they are recovering from depolarization and before their relaxation state [10].

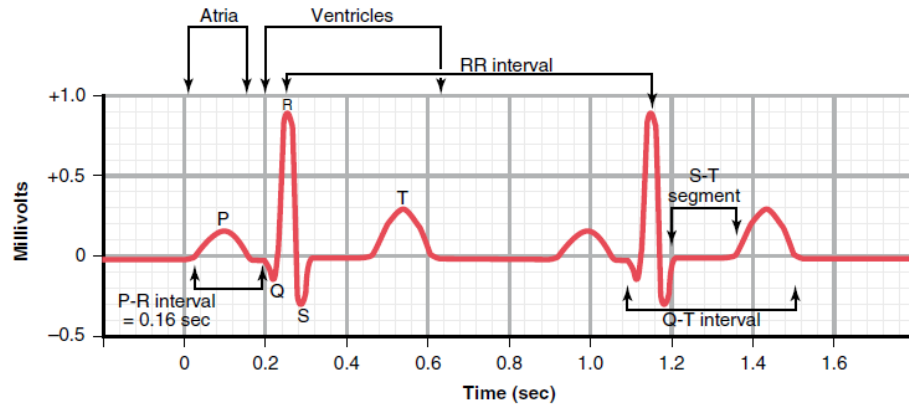


Figure 2.5: Electrocardiogram (ECG). Shows the polarization (P and QRS complex) and repolarization (T) waves [10].

Various lead configurations are used to record the ECG to capture the heart's electrical activity. Each ECG lead is a pair of electrodes (positive and negative) connected to the terminals of a recording machine, known as electrocardiograph. These leads could be bipolar or unipolar. The first ones use both electrodes placed on different parts of the body surface to do the measurement. The unipolar leads use the positive electrode on the body, and the negative is computed as a mathematically averaged central terminal [11].

There are three primary lead setups for capturing the ECG [10, 11] :

- The *three bipolar limb leads* take the left arm, right arm, and left leg as places to put the electrodes, as shown in **Figure 2.6a**. The measurement uses two extremities with electrodes of different polarity connected to the same electrocardiograph. By combining the three limbs it can be obtained three leads (I,II,III).
- The *augmented unipolar limb leads* use the same limbs. However in this configuration, two limbs are attached to the same negative terminal, and the other is connected to the positive. Three leads can be acquired: aVR, aVL and aVF (see **Figure 2.6b**) by changing the extremity used to place the positive electrode.
- The *precordial leads* use nine points, where three are the same limbs used in the other configurations, but in this case, they are connected to the negative terminal of the recorder to compute the reference electrode. The other six points are placed across the chest, as seen in **Figure 2.6c**. To acquire the ECG, the positive electrode alternates in these positions to obtain the V1, V2, V3, V4, V5 and V6 leads.

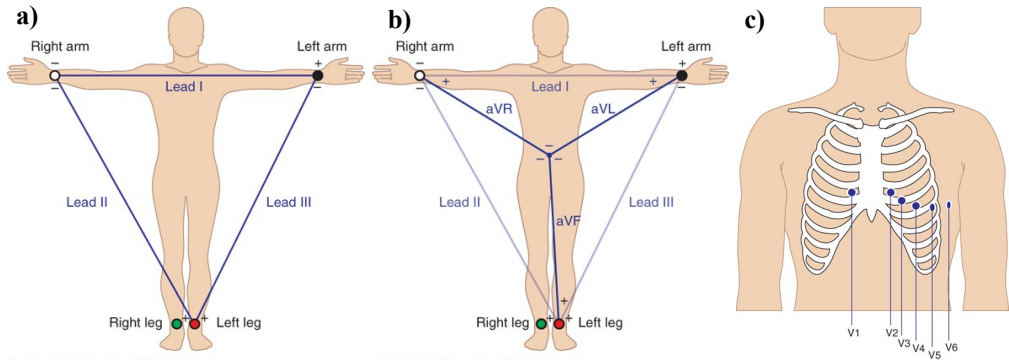


Figure 2.6: ECG leads configurations: a) Augmented unipolar limb leads the three bipolar limb leads, b) There is the augmented unipolar limb leads overlapped with the first configuration , c) Position of electrodes for the precordial leads [11].

Each lead configuration can be used separately. However, combining them to do an ECG acquisition of 12 leads is very common. In this way, a three-dimensional analysis of the cardiac electrical system can be done. The first two configurations allow to analyze the frontal plane, and the precordial leads make a scan in the horizontal plane [11].

2.1.2 Blood vessels

After the left heart pumps, the blood is ejected to reach every organ in the human body. This can be done thanks to the blood vessels performing the channel's function to transport it. They can be classified into arteries, arterioles, capillaries, venules, and veins (see **Figure 2.7**). Each of them is responsible for a distinct function as well its physical dimensions and morphological characteristics are also different [6].

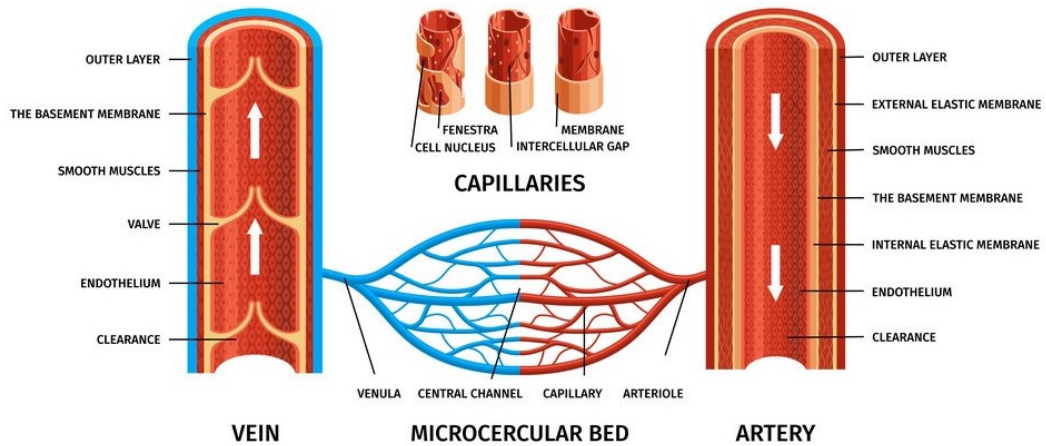


Figure 2.7: Blood vessels and the blood course throughout them starting in the arteries, arterioles, capillaries, venules and finally veins.

When the oxygenated blood leaves the heart, the arteries are the first type of vessels found. These have an internal monolayer of endothelial cells, as well as all types of vessels, and thick walls composed of smooth muscle, elastin, and collagen fibers. The elastin fibers can be stretched to twice their unload length, allowing the arteries to expand under increased pressure. That is why they can accept blood during systole and contract in diastole. The largest artery is the aorta, and with each branching, the arterial diameter decreases until the blood

reaches the arterioles, which act as resistances to regulate the blood flow. This is because arterioles have thicker walls with less elastic materials and more muscle. Then there are the capillaries, which are the smallest vessels, but together, they are the ones with the largest surface area, allowing them to be the exchange vessels of the cardiovascular system where the material trades between the blood and the interstitial fluid [6, 7].

At that point, the blood is deoxygenated and begins its return travel to the heart. After the material exchange in capillaries, the blood flows through the venules and veins that, contrary to arterioles and arteries, have thin walls, and consequently, their diameter can easily change in response to the changes in the pressure difference across the inside and outside of the vessel wall. In addition, the veins, especially the largest, have one-way valves to avoid the reverse flow. Later, the blood arrives at the heart, the blood volume depends largely on the veins, which due to their great distensibility, act like capacitance vessels and contain the 50% of the total blood volume [6].

As noted above, the blood flow is an essential characteristic of the blood which is used to describe each step that follows during the cardiac cycle. The blood flow can be calculated by modeling the blood vessels as a cylindrical tube of length L and an internal radius r , dependent on the type of vessel and the amount of these. Although the fluid flow also depends on other elements, how could be appreciated in **Equation 2.1** and **Equation 2.2** [6],

$$Q = \frac{\Delta P}{R} \quad (2.1)$$

$$R = \frac{8L\eta}{\pi r^4} \quad (2.2)$$

where Q is the flow rate, ΔP is the differential pressure between the inlet and outlet ends of the tube, which is the driving force of the fluid flow through a pipe, and R is the vascular resistance, which means the opposition to the fluid flow generated by intrinsic parameters of the blood vessel and the blood. This resistance depends on the tube's length, radius, as well as the fluid viscosity η , in this case, the blood [7].

It is important to clarify that blood flow differs from velocity. While the first one measures how much blood (volume) is passing through a segment in an interval of time, the second describes how long the blood has traveled in the same interval of time. **Equation 2.3** shows how to calculate the velocity of the flow:

$$\dot{V} = \frac{Q}{A} \quad (2.3)$$

where \dot{V} is the velocity of the flow, expressed like the relation between the flow rate Q and the total transversal area A of the tube. Considering these equations, it could be described in terms of velocity the path that follows the blood. The highest velocity is at the aorta and slowly decreases along the cardiovascular system until the blood reaches the lowest velocity into the capillaries. These are the smallest vessels but at the same time are the most numerous, making their total transversal area 1000 times higher than the aorta's area. After that, the flow velocity gradually increases in the veins up till the heart is reached [7].

2.1.3 Blood

The blood is a liquid equivalent to 8% of the body weight and is mainly composed of plasma, that is a solution of electrolytes and proteins, such as albumin, that plays a vital role in the exchange of materials. It is approximately 55% of the total blood volume, while the blood cells and other minor components are the rest of it [7]. The percentage of cells is referred to as hematocrit and is calculated with **Equation 2.4** [6].

$$H = \frac{V_{cells}^{\rightarrow}}{V_{blood}^{\rightarrow}} \quad (2.4)$$

where H stands for hematocrit, V_{cells}^{\rightarrow} is the blood cells volume and V_{blood}^{\rightarrow} is the total blood volume. The blood cells are divided into three types: platelets, leukocytes or white cells, and the erythrocytes or red cells.

The platelets are cells without nuclei formed in the bone marrow. Their average concentration is between 150.000 and 300.000 cells per microliter. Platelets are known due to their importance in the blood clotting process, thanks to the surface of their cell membrane, which has a covering of glycoproteins that causes adherence in damaged areas of the vessel walls, but the normal endothelium is repelled to prevent the formation of thrombi [10].

The leukocytes are typically found in concentrations around the 7.000 cells per microliter. They are part of the body's protective system, and their primary functions involve locating and eliminating threats to defend the body from infections, inflammation, and tumors [7].

Erythrocytes are the most concentrated type of cell in the blood with a range of 4.8 to 5.4 million cells per microliter [7]. Their primary function is to transport hemoglobin, which entails transporting oxygen from the lungs to the whole body. They also contain a high quantity of carbonic anhydrase that catalyzes the reaction between CO_2 and water to form bicarbonate ions (HCO_2^-). In this way, the blood

transports the CO_2 from the organs to the lungs and is finally expelled into the atmosphere [10].

The plasma is a conductive fluid, and the erythrocytes are highly resistant. While the other types of cells are insignificant due to their small size or number. The resistivity in the blood is highly correlated with the hematocrit, so the greater the number of blood cells, the higher the resistance. Also, there is a dependence on the erythrocytes' orientation because they are oval-shaped, and the resistance is more significant in the larger axis. Therefore, when the blood is static, the cells are randomly oriented, and the resistivity is isotropic. Meanwhile, when there is a blood flow, the red cells are aligned with the flow, and the resistance is anisotropic [12].

Currently, the direct relation between the electrical resistance and volume is not defined. However, some studies such as *A.L. Zuev*(2021)[13], found that the resistivity in the blood vessels is strongly influenced by changes in cross sectional area. With a larger area, smaller is the electrical impedance.

2.2 Cardiovascular diseases and arterial stiffness

As described above, the cardiovascular system combines several subsystems involving mechanical, electrical, chemical, and physical processes. All of these must work synchronized and proportionately to enable the system to function correctly. The failure of any of their mechanisms or elements of them could produce a cardiovascular disease (CVD).

The CVDs, according to the World Health Organization (WHO), are the first cause of death globally. These diseases, which involve disorders in the heart and the blood vessels, take around 17.9 million lives each year. In the European Union (EU), more than €210 billion was spent in 2015, including the healthcare costs and the productivity losses [14].

There are several CVDs, such as heart failure, ischemic stroke, myocardial infarction, among others. Each of them has its own etiology and risk factors, but the most common denominator is the development of atherosclerosis [15].

Atherosclerosis is characterized by the accumulation of lipids and fibrous elements inside the walls of the large arteries due to endothelial damage, leading to adhesion molecules called foam cells. The arteries' structure and how lipids and monocytes' buildup form fatty streaks, are shown in **Figure 2.8**. Over time, their aggregation forms a plaque, which increases to block the blood flow, or the injury can explode and generate a thrombus [10, 16].

Thrombus and the block of the blood are not the only problems generated.

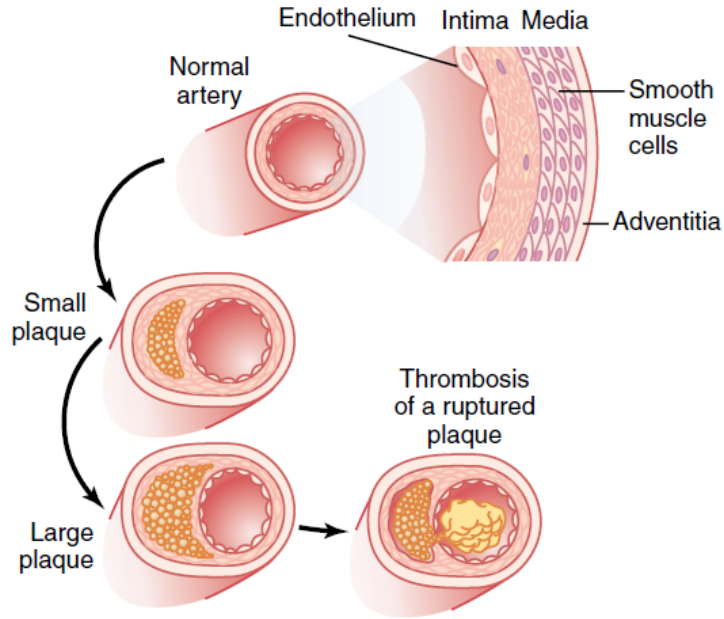


Figure 2.8: Artery structure and development of the atherosclerosis [10].

Atherosclerotic arteries also experience a significant distensibility loss, known as arterial stiffness.

The distensibility plays a marked role in the relationship between pressure and blood flow due to the capacitive effect of the artery. The stiffening of the walls leads to decreased artery storage capacity, which involves increasing the pulse wave propagation speed. These factors could develop hypertension, especially in the elderly, and therefore, the cardiovascular risk is increased. So, the measurement of the arterial stiffness is necessary for the early diagnosis of CVDs. The arterial pulse wave velocity (PWV) has emerged as a predictor of cardiovascular morbidity and mortality as well as a factor of cardiovascular risk [17].

2.3 Pulse Wave Velocity

The velocity at which the pulse wave spreads along the arterial system is known as Pulse Wave Velocity (PWV), and it is considered as a biomarker because it evaluates the elastic properties of the arteries. If the vessel has a high distensibility and compliance, more blood is stored; thus, there is less blood flow and, in turn, a lower speed. Therefore, higher PWV implies more significant arterial stiffening [4].

Different types of waves have been used to compute the PWV, but the pressure wave or Pulse Wave (PW) is one of the most common, so it is essential first to understand what it is.

2.3.1 Pulse Wave

The Pulse Wave or arterial pulse is a fundamental vital signal obtained from the pressure pulsation, which is a pressure wave generated in the arterial walls when the impulse generated in the systole moves the blood forward. In **Figure 2.9** is shown a typical pulse wave at the aortic arch. The pressure pulse peak occurs when the ejection happens during the systole, then has a sharp drop until the dicrotic notch, when the aortic valve closes, and a slight increment happens. During the diastole, the pressure slowly decreases to rise again when the next systole starts [7, 10].

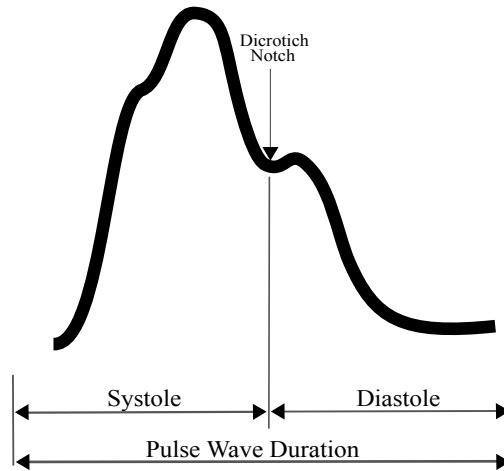


Figure 2.9: Typical pulse waveform in aortic arch.

The PW can be detected in several sites (see **Figure 2.10a**), but these present changes in the signal morphology, which means in amplitude and form. The more peripheral the site, the more the pulse pressure increases due to the systolic and diastolic pressure decrease, but the diastolic does it more abruptly. Also, the dicrotic notch appears later, which implies a temporal delay among the signals, as shown in **Figure 2.10b**, where two PWs were acquired at different points [7, 18].

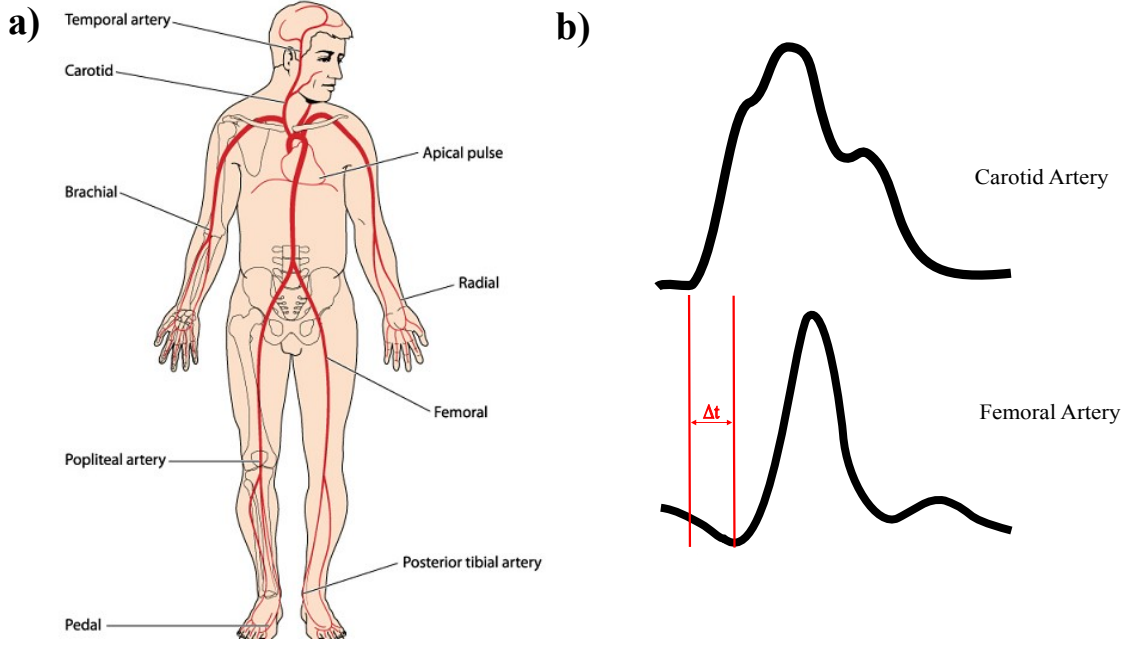


Figure 2.10: a) Collecting sites for the arterial pulse [19], b) Morphological and temporal differences between the PW in the carotid and femoral artery.

2.4 PWV estimation

As mentioned previously, the PWV describes the elasticity of the arteries. However, these properties change along the arterial system. For this reason, the PWV provides general or specific information depending on the measurement modality. The measurement is carried out locally if detailed information about a single segment is needed, but it is done regionally to give general information about the arterial tree distensibility [4].

The local measurement is made on just one artery, taking two acquisition points with a small distance between them. In contrast, the PW is obtained in two different arteries for the regional measurement. Despite their differences, both follow the **Equation 2.5** [4]:

$$PWV = \frac{\Delta L}{PTT} \quad (2.5)$$

where ΔL is the distance between the two acquisition points, and the PTT is the Pulse Transit Time, which can be calculated in two ways. The first is computing the time delay between both signals, as shown in **Figure 2.10b**. The point to

assess the PTT can be chosen at any spot of the PW [3]; however, the foot of the wave is the most common. The second option, most used for regional measurements, needs an ECG as a reference point. In this method, as shown in **Figure 2.11**, the PTT is computed for both PWs relative to the R wave of the ECG, obtaining PTT_1 and PTT_2 , and then the PTT for the PWV is computed by subtracting the PTT of the nearest vessel to the distal site's PTT [20].

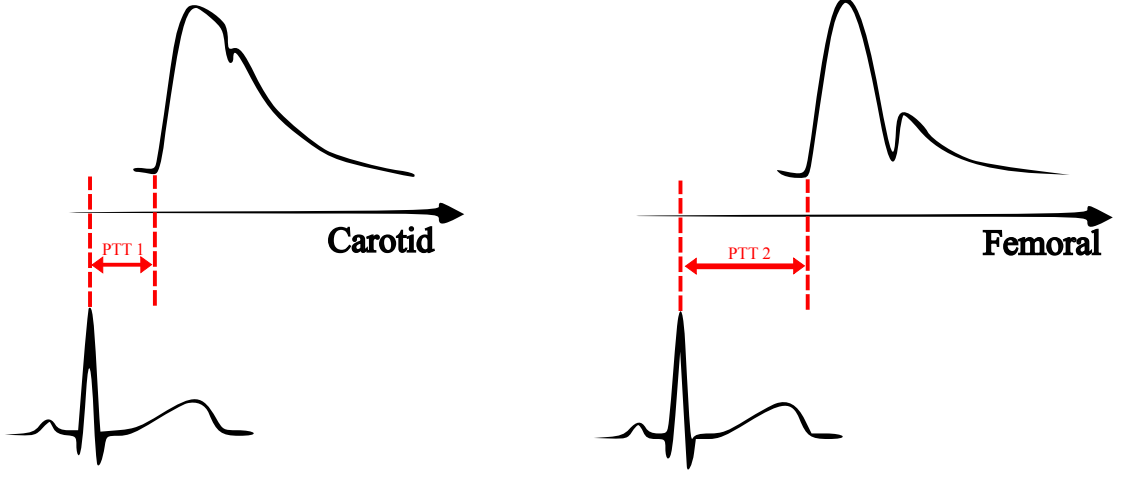


Figure 2.11: PW acquired in carotid and femoral arteries; and PTT assessment with ECG as reference.

When the PWV is computed at regional level, **Equation 2.5** must have a minor modification because the path that follows the blood between the measuring sites is not a straight line, so a correction factor is added. The carotid-femoral measure is the most widespread pair of sites to assess the PWV, and a correction factor of 0.8 is used [3]. So, **Equation 2.6** describes the carotid-femoral PWV (cfPWV).

$$cfPWV = 0.8 * \frac{\Delta L}{PTT} \quad (2.6)$$

Irrespective of the method used to measure the PWV, it can be related to the vessels' distensibility and arterial stiffness, using **Equation 2.7** and **Equation 2.8**, known as the Bramwell-Hill equation [3]:

$$D = \frac{\partial A}{A \partial P} \quad (2.7)$$

where D stands for distensibility, A for the cross-sectional area, and P for pressure. Therefore, the distensibility can be defined as the cross-sectional area's relative responsiveness to pressure changes [3].

$$PWV = \sqrt{\frac{A}{\rho} \frac{\partial P}{\partial A}} = \sqrt{\frac{1}{\rho D}} \quad (2.8)$$

In the Bramwell-Hill equation, ρ is the density of the liquid. If it is considered constant, the PWV has an inversely proportional relationship with the root square of the distensibility in such a way that a decrement in the distensibility translates into a high increase in the velocity [21].

In this way, the clinical devices compute the PWV and its relationship to the arterial elastic properties, always considering that depending on the analysis level (regional or local) and the sites used, the PWV can take different values and not necessarily be pathological.

2.4.1 Clinical devices

The current devices used clinically are divided into imaging and electromechanical devices. However, almost all devices use the two points for PW acquisition and the posterior PTT assessment. The PW obtained by the devices are flow or pressure waves, which contain the required information to detect the superimposed PW [4, 22].

Magnetic Resonance Imaging (MRI) and Ultra Sound(US) are the two techniques used in the imaging devices for PWV measurement. In MRI cases the measurement is done locally, and the PW can be obtained in several ways, but one of the most utilized uses the contrast changes in the images to acquire it. Both points are in the same vessel, as shown in **Figure 2.12a**, and a center line is drawn in the artery to measure the distance [22]. On the other hand, the US devices can do the measurement whether locally or regionally. In whichever case, the Doppler effect is used to acquire the PW, and in some cases, as **Figure 2.12b** shows, the US is synchronized with an ECG to do the measurements [23].

The electromechanical devices are the gold standard for PWV measurement. They all acquire regionally and establish direct contact with the skin at the artery site.

The *Pulse Pen*[®] and the *SphygmoCor*[®] are based on the applanation tonometry principle. The sensor is placed over the skin where the artery is located. Then, a slight pressure is applied, and the artery is compressed. The PW is recorded with the balance of the pressures generated by the operator and the artery on the sensor

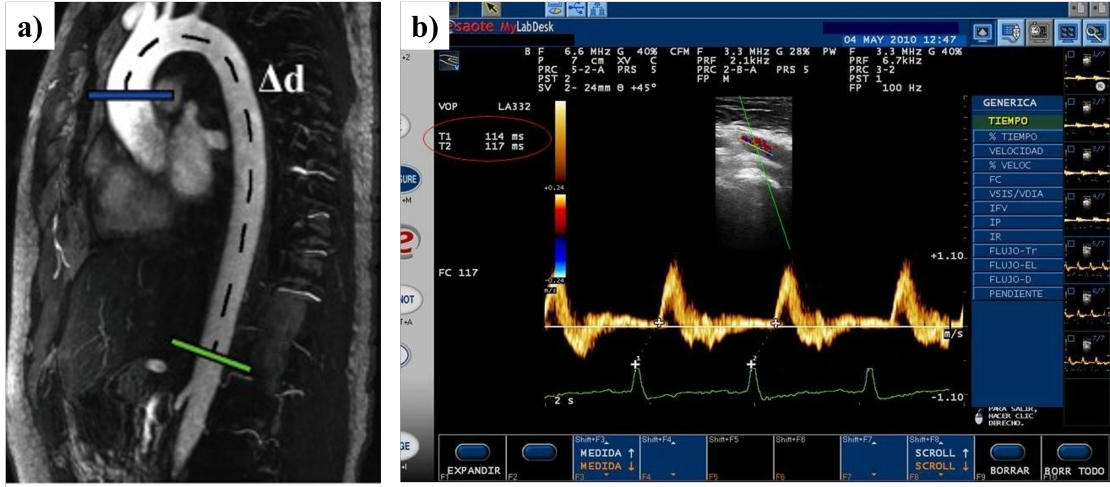


Figure 2.12: Imaging techniques for PWV measurement. a) MRI at the aortic arch [22]; b) US at femoral artery synchronized with ECG [23].

(see **Figure 2.13**) [20]. The *Pulse Pen*[®] uses two tonometers and the ECG, while the *SphygmoCor*[®] uses just one tonometer and a femoral cuff, which captures the PW based on volumetric displacement [24].

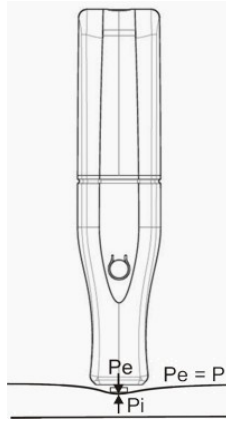


Figure 2.13: Tonometry sensor [20].

Complior[®] uses two sensors based on a piezoelectric pressure mechanotransducer. One probe is attached to the neck, with a kind of clamp, positioning the sensor over the carotid, and the second probe is pressed by the operator at the femoral artery [4]. Equal to the tonometer, this sensor acquires the PW based on the pressure changes. The last clinically approved device is *Arteriograph*[®], the only one that uses just one acquisition point. With one cuff at the arm, this device records the

PW. Then, the PTT is measured between the first and the second peaks of the wave, where the first peak corresponds to the systolic peak, and the second is from the reflected systolic wave. Finally, twice the distance from the jugulum to the symphysis is utilized to compute the PWV [25].

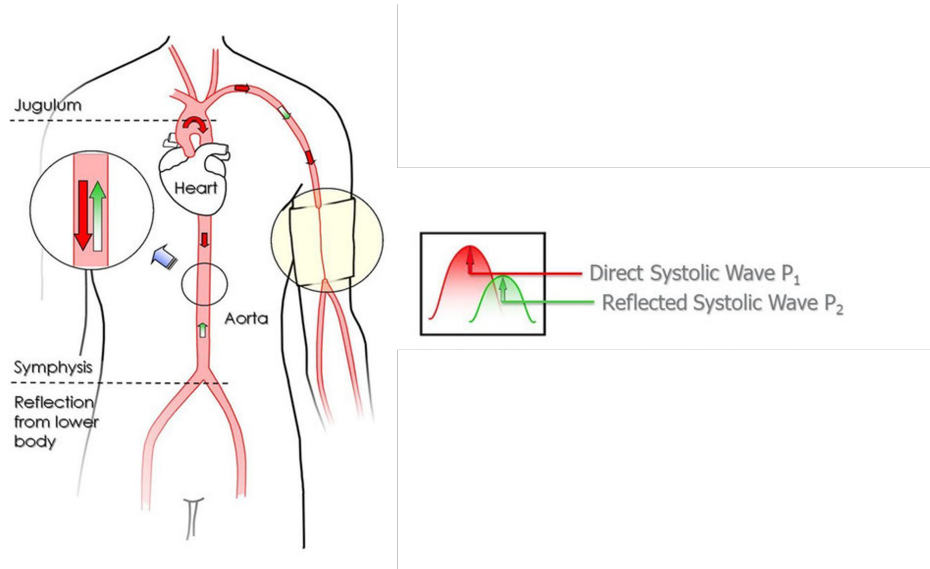


Figure 2.14: *Arteriograph*[®] device. Use of one acquisition cite for PWV measurement [25].

Although all these devices are widely used, the imaging and electromechanical devices require high-cost equipment. For this reason, some cost-effective devices have been developed, such as the *Athos* of I. Buraioli, et al. [26], which use two pressure sensors encapsulated in two pen-shaped supports placed at the carotid and femoral arteries to evaluate the PWV, providing the possibility to do it with or without ECG.

The electromechanical devices, even the recently developed ones, are susceptible to changes in the pressure applied to the arteries or to the angle between the artery and the sensor, so the waveform could be damaged or distorted [4]. Additionally, because of their operating principle, any current devices or sensors cannot be used for wearable and continuous monitoring. Therefore, novel solutions are emerging to try to solve these problems, among which are non-invasive ways of acquiring the PW, such as plethysmographic methods.

2.5 Plethysmography signal

Plethysmography is defined as the measurement of changes in volume, and it is very helpful for the cardiovascular systems analysis [27]. It is essential to clarify that the signals acquired by plethysmography are flow (volume changes) waves, not pressure waves. Nevertheless, as mentioned previously, the morphological resemblance (systolic peak, dicrotic notch, diastolic run-off) between them allows to use it as PW [28].

The optical principle is maybe the most common among those to measure the plethysmographic signal, and it is known as photoplethysmography (PPG), has been widely utilized in medical devices as the pulse oximeter or digital beat-to-beat for blood pressure measurement [29]. However, other physical principles can be related to volume variation, such as impedance plethysmography (IPG) that relies on the measurement of the body's electrical properties.

2.5.1 Impedance Plethysmography (IPG)

The IPG is a non-invasive measurement of the PW that takes advantage of the electrical properties of the tissues as the internal impedance, which can be represented with **Equation 2.9** [21]:

$$Z_x = \frac{\rho_x L}{A_x} \quad (2.9)$$

where Z_x stands for the tissue's impedance, ρ_x is the tissue resistivity, L is the length of the evaluated segment, and A is the cross-sectional area of the tissue. Therefore, the complex tissue-blood can be modeled, as shown in **Figure 2.15**, as two resistors in parallel: Z_b for the blood impedance and Z_0 for the adjacent tissues impedance. The computing of the total impedance Z follows **Equation 2.10** [21].

$$\frac{1}{Z} = \frac{1}{Z_0} + \frac{1}{Z_b} \quad (2.10)$$

The Z_0 is considered constant because there are no significant changes in the impedance of the tissue surrounding the arteries. So, the total impedance (ΔZ) changes should be due to the Z_b variation. Therefore, from the previous equations and consideration it can be obtained the **Equation 2.11** that compute the cross-sectional area variation (ΔA), and hence the volume changes:

$$\Delta A \approx \frac{\rho_b L \Delta Z}{Z_b^2} \Rightarrow \Delta V \approx \frac{\rho_b L^2 \Delta Z}{Z_b^2} \quad (2.11)$$

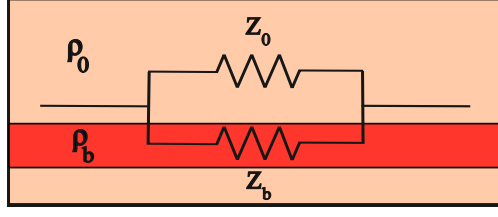


Figure 2.15: Impedance model of the blood and its surrounding tissue

IPG usually does the measurements using an array of four electrodes placed along the vessel (see **Figure 2.16a**). The outer electrodes inject a fixed alternating current, and the internal electrodes perform the voltage measurement [5]. In this way, the impedance can be computed using **Equation 2.12**.

$$Z = \frac{V}{I} \quad (2.12)$$

where V is the voltage and I is the current injected. The signal acquired (see figure **Figure 2.16b**) must be demodulated to remove the AC component. After this, two components remain: The DC component which represent the basal impedance of the segment, and a pulsatile component, which represents the cardiac behavior [5].

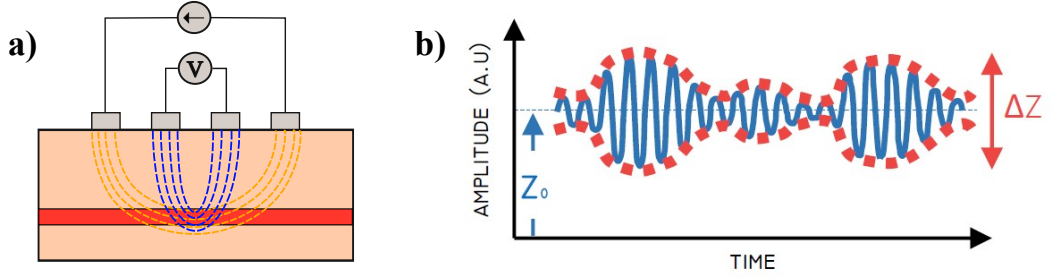


Figure 2.16: a) Electrodes placement for IPG acquisition. Outer electrodes inject current and inner electrodes measure the voltage; b) IPG signal with its AC (blue), DC (Z_0 offset) and the pulsatile (red) components [5].

Previous studies have used the IPG to acquire the PW with the aim of measuring the pulse rate, as J. He, et al. [30], which have reached to obtain the expected pulse wave in the radial artery when the subjects keep the arm still, but when there are movements, the system has to be re-adjusted. Other studies, such as the one by T. Huynh, et al. [21], have measured the PTT to estimate the blood pressure using an IPG sensor and another for PPG, and have concluded that the best location for

impedance measurement is the radial artery because it is one of the most superficial vessels and the electric current can reach it. Finally, A. Wiegerinck , et al. [31] measured the PWV, obtaining good results. However, they used the ECG and one point for the IPG to compute the PTT and then calculate the velocity. None of the studies found have used two sites to acquire the IPG for PWV measurement, except for the K. Lee & H-J. Yoo study [32]. They have reached to acquire the PW signals at the radial artery and the aortic arch, measuring the PWV continuously for 95 minutes. The only drawback of the developed system is that it needs eight electrodes to get the signal in the aortic arch, which makes it uncomfortable for the subjects.

Chapter 3

Materials

In order to acquire the PW using the IPG, in this project was used the microcontroller ADuCM355 as main acquisition device. In addition has been used other devices as the Raspberry Pi 3 for data transmission and storage, the NiDAQ USB-6259 as alternative for the signal acquisition, and the g.HIAMP which was used for ECG recording.

3.1 ADuCM355

The Analog DevicesTM has developed the ADuCM355 which is a system on a chip intended to control electrochemical sensors and biosensors. For the purpose of this project it was used the evaluation board EVAL-ADuCM355QSPZ shown in **Figure 3.1** [33].

The chip features a 16-bit analog-to-digital converter (ADC), a high speed digital-to-analog converter (DAC), and a number of communication peripherals, such as serial peripheral interface (SPI) and universal asynchronous receiver/transmitter (UART).

The ADC operates with a conversion rate of 800 kHz or 1.6 MHz, and an input range of -0.9 V to 0.9 V . Additionally, it includes current inputs through trans impedance amplifiers (TIA) with programmable load resistor. The high speed DAC was designed for impedance measurements and allows outputs signals with frequencies up to 200 kHz.

The ADuCM355 includes a digital subsystem with several post-processing features for the ADC result, such as low-pass and notch filters, programmable averaging and statistics of ADC and the Discrete Fourier Transform (DFT). Among

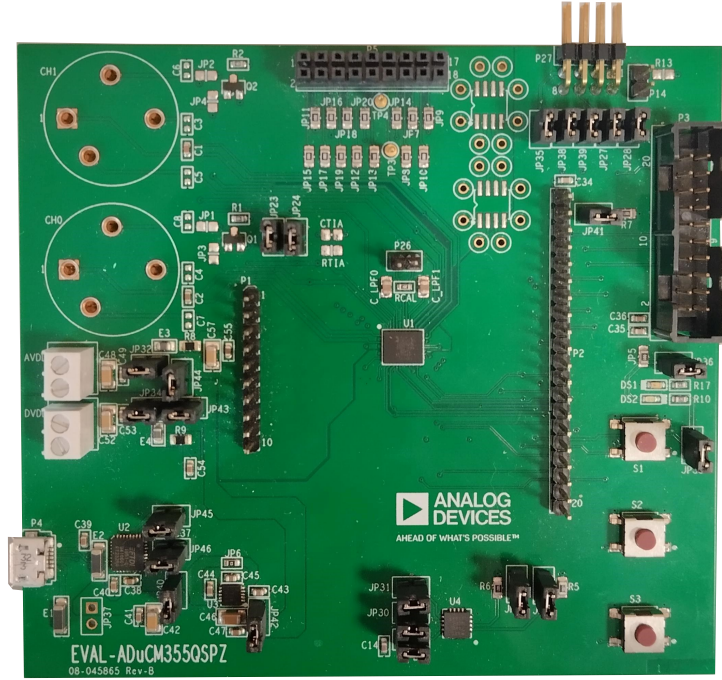


Figure 3.1: EVAL-ADuCM355QSPZ evaluation board

the low-pass filters, the Sinc3 is the one strongly recommended to be used by the manufacturer. It is a digital filter with programmable number of samples (2, 4 or 5 samples) to apply the filter. The DFT is used for impedance measurement, and can be implemented using from 4 to 16384 samples.

One of the main features of the ADuCM355 is that includes a system which has been specifically designed for impedance measurement.

The ADuCM355 is programmed in C, so the recommended Integrated Development Environment (IDE) by the manufacturer was used. The IAR[®] Embedded Workbench for Arm, that supports the ADuCM355's processor (Arm[®] Cortex[™]-M3), has been used for this purpose.

3.1.1 Impedance measurement system

Contrary to many impedance measuring devices, the ADuCM355 imposes a fixed voltage and measures the corresponding current. The analysis can be performed in both bipolar or tetrapolar configuration. In **Figure 3.2** a simplified representation of the ADuCM355 measuring system is shown.

The system is divided into four macro-blocks:

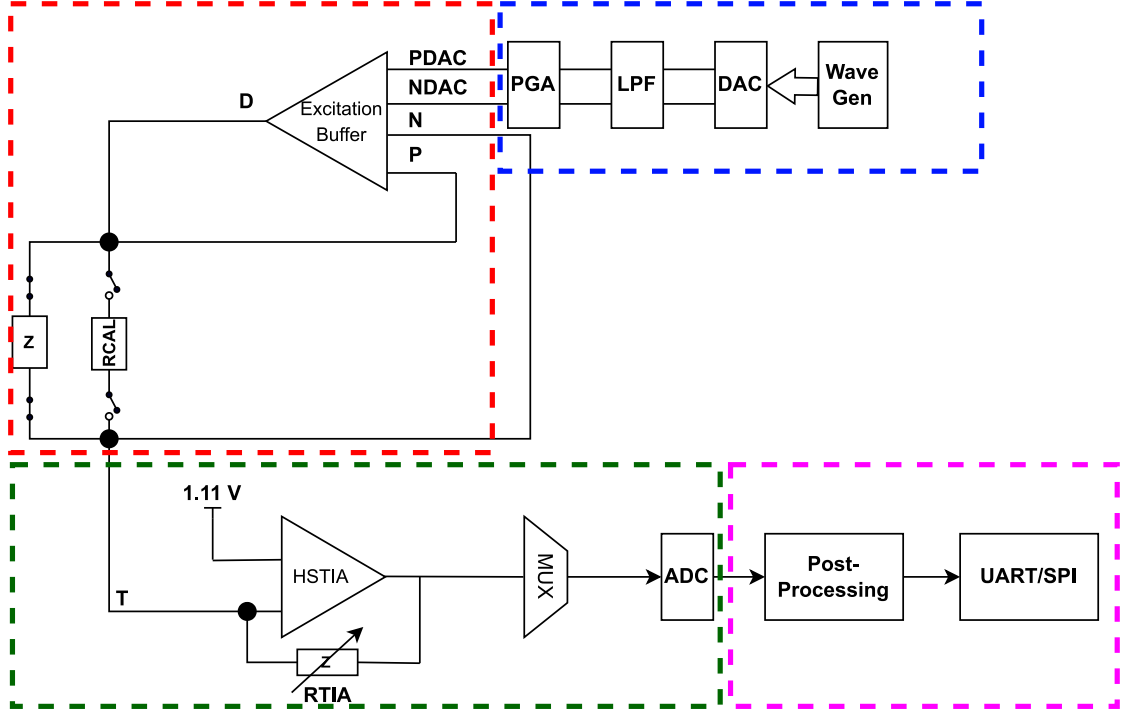


Figure 3.2: Simplified system for impedance measurement of the ADuCM355. Highlighted in blue dashed line is the Waveform generation macro-block, in red the voltage injection, green the current measurement, and magenta the post processing.

1. **Waveform generation:** This macro-block is constituted of a Waveform Generator (WG), a 12-bit high-speed DAC, a low-pass filter (LPF) block, and a programmable gain amplifier (PGA) that has a maximum gain of two. The WG generates a digital sinusoidal wave with a maximum amplitude of 600 mV peak-to-peak and a frequency of up to 200 kHz. Then, the wave is converted in the DAC to analog. The signal is passed through the LPF to remove high frequency noise, and then it is amplified with the PGA, reaching voltages up to 1.2 V peak-to-peak. The generated signal has the P_{DAC} and N_{DAC} pins as the output of this macro-block.
2. **Voltage injection:** The excitation amplifier buffer (EAB), as well as a set of switches and impedances Z to be measured, compose this macro-block. Different Z loads can be connected and measured individually by activating the corresponding switches. Even the evaluation board includes a resistor of $200\ \Omega$, which is connected to the switches called R_{CAL} .

The EAB has four inputs: P_{DAC} , N_{DAC} , P , and N . The P_{DAC} and N_{DAC} are the wave generation macro-block outputs. P and N are the pins where the Z

load is connected. This amplifier must ensure that the differential amplitude of the PDAC-NDAC inputs is the same as that of P-N. That means the voltage drop in Z must equal to the one at the generated in the previous macro-block. The EAB has an output that injects the corresponding current to Z to ensure that. The output of this block is the current that passes throughout Z .

3. **Current measurement:** The macro-block is conformed for high-speed TIA, a multiplexer, and ADC. The TIA converts the current to a voltage, and its amplitude depends on the magnitude of the resistor R_{TIA} , which can be modified internally or externally. The multiplexer just has the function of selecting the TIA as the ADC input. The 16-bit ADC converts the signal into digital, which is this block's output.
4. **Signal processing:** This macro-block has two components: the post-processing block and the communication block. In the first, there are all the filters that could be applied to the signal, such as notch or low-pass filters. In the second are the peripherals to transmit data via UART or SPI.

3.1.2 Communication protocols

The ADuCM355 also features the communication peripherals SPI and UART, which were used in this study to send data obtained with the microcontroller to an external computer or a Raspberry.

The SPI is a synchronous serial communication with which the ADuCM355 can perform as master or slave with a maximum bit rate of 6.5 MHz. This interface allows to transmit and receive eight-bit messages, even at the same time. In this project, the chip was used as slave. In **Figure 3.3** is shown how the ADuCM355 should be connected for the SPI communication with an external device.

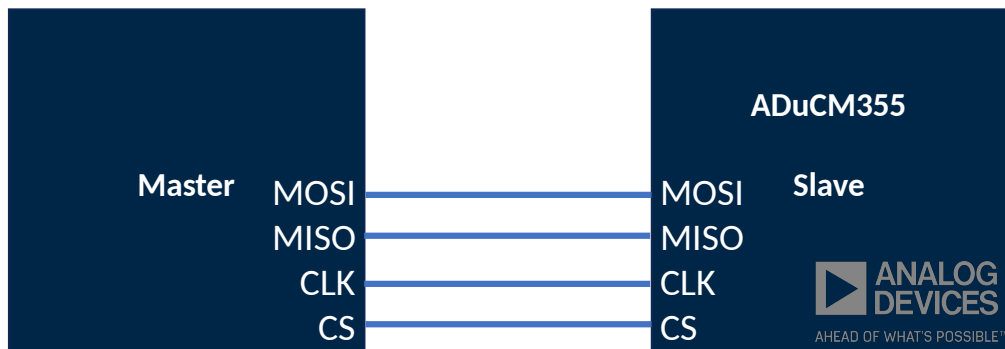


Figure 3.3: ADuCM355 connection to a external device for SPI communication

The SPI communication requires four connection channels: The Master Out Slave In (MOSI), Master In Slave Out (MISO), the serial Clock (CLK), and the Chip Select (CS). The MOSI and MISO are the channels for the data exchange; CLK is the clock signal channel to synchronize both devices, and CS is the channel that, when activated, allows communication between them. In **Figure 3.4** is shown how the communication works.

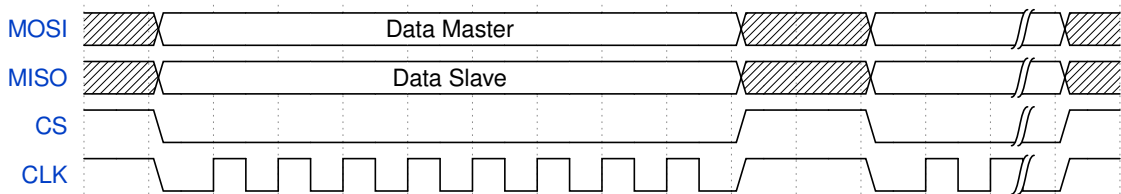


Figure 3.4: SPI communication protocol

The CS activates the communication when its logical value is low. At that moment the CLK sends eight clock pulses, while, the Master and Slave send 8-bit messages via the MOSI and MISO channels respectively. Each clock pulse reads one bit of the MOSI and MISO. When the eight pulses have finished, the CS is set high, stopping the data transmission. The communication will resume when the CS is set to low again. The Master device decides the time between the transmission of a message and the next one.

The UART is an asynchronous serial communication protocol that allows the transmission or reception, of messages of various lengths, with a maximum baud rate of 230400. In this case, the evaluation board has a UART-USB converter, which facilitates the connection with an external computer. However, the UART communication actually uses two channels to exchange information, as shown in **Figure 3.5**.

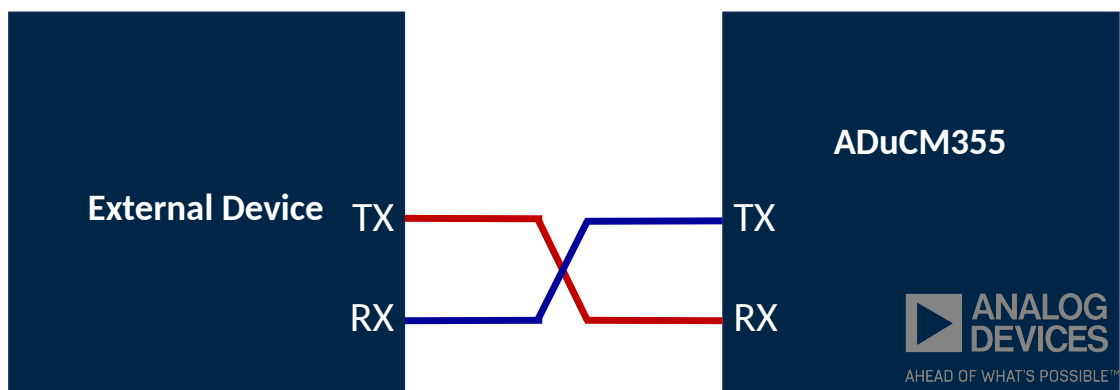


Figure 3.5: ADuCM355 connection to a external device for UART communication.

3.2 Raspberry

It was utilized the Raspberry Pi 3 Model B (see **Figure 3.6**) as an external computer. It features 1 GB RAM, wireless LAN, and Bluetooth connection, four USB ports and diverse peripheral interfaces [34]. Therefore, it performs the computer functions and adds other functionalities such SPI communication. It was used as the master in the communication with the ADuCM355 because it just permits this operation mode. Also, it was exploited the UART communication and its storage capacity.

The Raspberry can be programmed using Python, so it was used its internal IDE called Thonny.

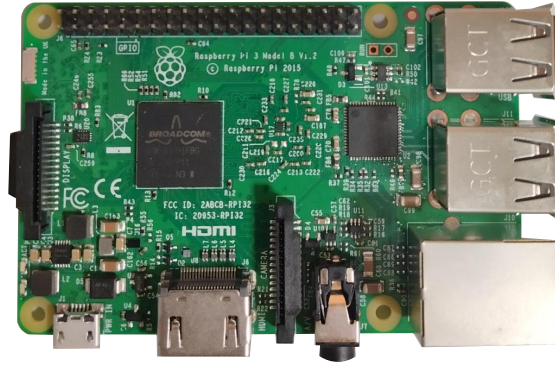


Figure 3.6: Raspberry pi 3 Model B

3.3 NiDAQ

For external ADC measurements, Ni 6259 was used from the National Instruments (see **Figure 3.7**). It features 16 differential input channels, a 16-bit ADC with a maximum sampling rate of 1.25 MS/sec, and an input range up to ± 10 V [35].

For the data acquisition, the *Data Acquisition Toolbox* of Matlab® was used, which is the support package for the National Instrument Devices.



Figure 3.7: NiDAQ USB-6259

3.4 g.HIAMP

The ECG was acquired to take a reference for the IPG measurement. In order to do it, the g.HIAMP from the Guger Technologies (g.Tec) was used. The g.HIAMP is a high-performance biosignal amplifier excellent for measuring bio-signals, such as the ECG or electroencephalography(EEG). It features 256 channels with the same number of ADCs of 24-bit, which can operate up to 38.4 kHz[36]. The signal recording is done with g.Recorder a software done by the g.Tec, which also permits the capture of the trigger information. The g.Recorder data can be exported to be post-processed in Matlab®.



Figure 3.8: g.HIAMP for ECG and EEG acquisition

Chapter 4

Methods

This thesis project used three methods to acquire the plethysmography signal measuring the impedance. The ADuCM355 was used in the three methods, and its impedance measurement system was exploited in different ways. The differences between the methods were relative to the point of the system at which the signal was accessed to complete its processing.

For all the methods, three tests were designed where the first test was the least difficult and the third the most complex. If the method did not pass any tests, it was not continued with the next one. A final proof to measure the plethysmographic signal in different configurations was designed for the methods that passed the three previous tests.

In each method, a fixed voltage signal was injected with a sinusoidal wave of 50 kHz frequency. It was selected because previous studies [30, 31, 32] have used this frequency, stating that at this frequency, the blood is more conductive than the surrounding tissues. However, the frequency was changed for some tests to facilitate the analysis.

The current passing through Z was always converted into voltage and then processed. The signal obtained contained the three typical components of the IPG exposed in **subsection 2.5.1**. In this project, the DFT was used as a demodulation method to extract the pulsatile component carried in the AC signal.

The DFT was used on the basis that there was only one frequency in the entire spectrum of the signal corresponding to the frequency of the signal injected. The amplitude of this peak will be proportional to the current passing through Z . However, this is not enough to compute the impedance value. Measure a reference impedance (R_{CAL}) is mandatory. With both DFT values, it is possible to calculate the unknown impedance with **Equation 4.1**

$$Z = \frac{||DFT_{R_{CAL}}||}{||DFT_Z||} * R_{CAL} \quad (4.1)$$

where $||DFT_x||$ stands for the DFT's magnitude for R_{CAL} and Z , and R_{CAL} is the reference impedance value. The ratio is inversely proportional, so the greater the current, the greater the DFT's magnitude and the lower the impedance. Following this logic, it was decided that the highest current should be obtained when R_{CAL} is measured, so it was chosen as R_{CAL} the reference resistance of $200\ \Omega$ included in the evaluation board of the ADuCM355 because it is lower than the expected bio-impedance, which should be over $1\ \text{k}\Omega$ [30].

The selection of the lowest impedance allowed is essential because it permits establishing the value of R_{TIA} to avoid that the maximum output of the TIA overloads the ADC.

4.1 First method: Internal sampling and processing of ADuCM355's

This method intends to use the internal ADuCM355's components to acquire the signal, do the post-processing, calculate the DFT, and compute the impedance. To achieve this, the recommended impedance measurement procedure by Analog DevicesTM was followed in the first instance.

The original procedure can be seen in the flowchart of **Figure 4.1**. Initially, the ADuCM355 generates the waveform to be injected. Then begins the R_{CAL} switches are activated. After, the ADC reads the signal, and each four samples the Sinc 3 filter is applied. The process is repeated n times, where n is the number of samples used to calculate the DFT. Finally, the DFT's magnitude for R_{CAL} is computed.

Afterward, the switches connected to the Z load are set, and the same process is executed to obtain the DFT's magnitude for Z . The Z value is calculated with both DFT's magnitudes using **Equation 4.1**. If a new Z measure is desired, it must be followed all the steps again.

Each step applied during the ADC post-processing directly affects the sampling frequency (F_s). In addition, to calculate Z , it is necessary to repeat all the process two times because it is always measured R_{CAL} . The **Equation 4.2** describes how each step influences F_s .

$$F_s = \frac{ADC_{rate}}{2 * Sinc3_{samp} DFT_{samp}} \quad (4.2)$$

where ADC_{rate} is the ADC's update rate set to $800kHz$, the $Sinc3_{samp}$ is the number of samples used for the Sinc3 filter, usually four, and DFT_{samp} is the samples used to calculate the DFT. In **Table 4.1** is summarized the F_s for different numbers of samples used for the DFT.

The maximum F_s reached was 24 Hz using 4096 points for the DFT, which is a very low frequency if compared with clinical devices that reach sampling rates on the order of 100 Hz to 2,000 Hz [22]. For this reason, it was decided to modify the original process to increase F_s , as shown in **Figure 4.1**.

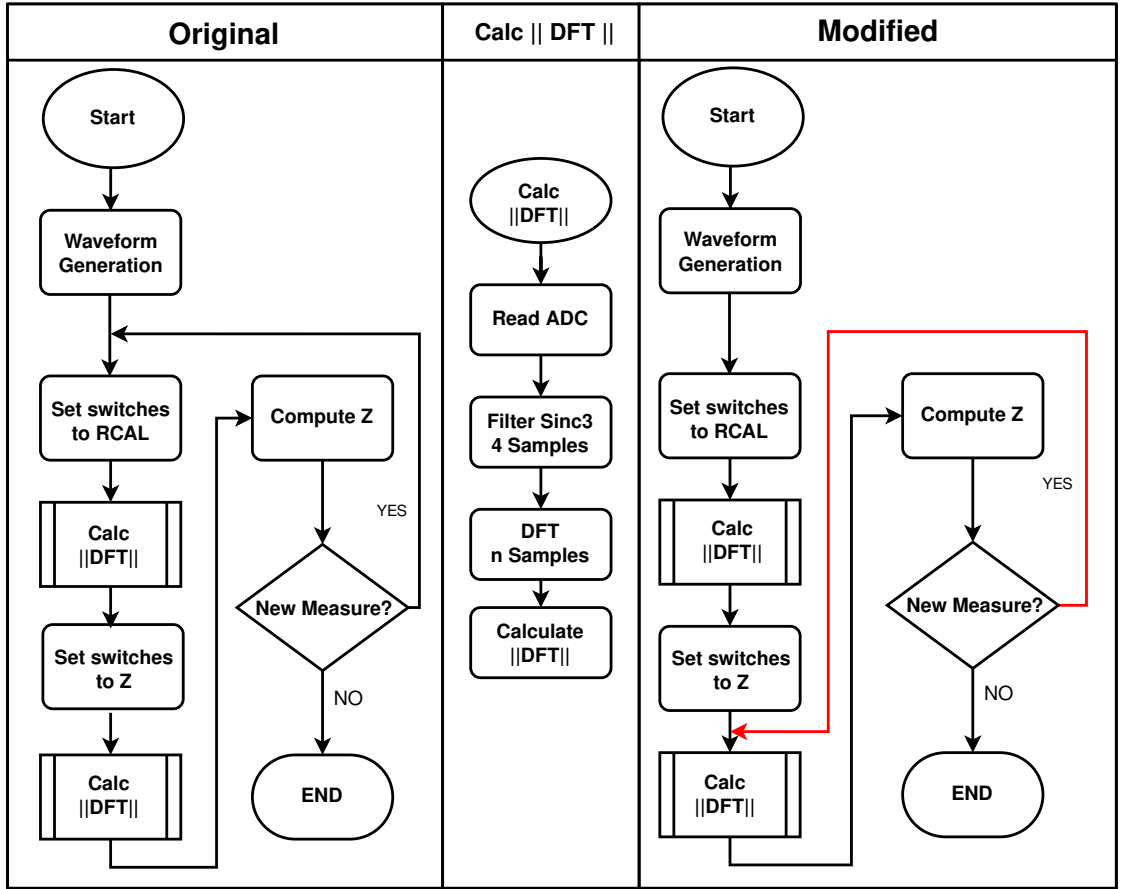


Figure 4.1: Flowchart of the first method . On the left is the original procedure and on the right is the process modified with the major change highlighted in red. On the middle is the sub-process to calculate the DFT's magnitude.

The main change in the pipeline is that the R_{CAL} just needs to be measured once, and its DFT magnitude is stored for later calculations of Z . In this way, the **Equation 4.2** suffers a slight modification, as seen in **Equation 4.3**:

$$F_s = \frac{ADC_{rate}}{Sinc3_{samp} DFT_{samp}} \quad (4.3)$$

where the factor "2" is removed in the denominator because the impedance measuring process involves just one DFT calculation and not two as in the original form. In **Table 4.1** are also reported F_s s for the modified process.

DFT_{samp}	F_s original	F_s modified
4096	24 Hz	48 Hz
8192	12 Hz	24 Hz
16384	6 Hz	12 Hz

Table 4.1: Influence of DFT's number of samples on the sampling frequency for the original and modified method.

Even with the modifications, the sampling rate remains low, with a maximum of 48 Hz. In addition, a high number of DFT points are desired to increase the measurement resolution because, according to other studies ([30],[31]) the impedance variation (ΔZ) is lower than 1Ω . Therefore, working with 8192 or 16384 DFT points would be better, that is, an even lower frequency. For those reasons, the two following methods were proposed aiming to increase the sampling rate.

The Z value obtained was sent via UART for external post-processing of the impedance signal. The corresponding filters were included in the post-processing according to the evaluated test.

4.2 Second method: NiDaQ sampling and external processing

This method intended to use the ADuCM355 to inject the voltage to the Z load, and the current measurement would be done externally to increment the sampling rate. Capture the TIA's output signal was proposed, which should be proportional to the current that passes through the load Z . On **Figure 4.2** is shown the setup for this second method to measure the impedance.

First, the impedance measurement system was modified. Initially, the R_{TIA} used is internal to the ADuCM355, but access to this resistor for measuring its voltage drop is not possible. Therefore, it was configured an external resistor, and the voltage measurement was done with NiDAQ USB-6259 with the ADC sampling rate of 500 kHz .

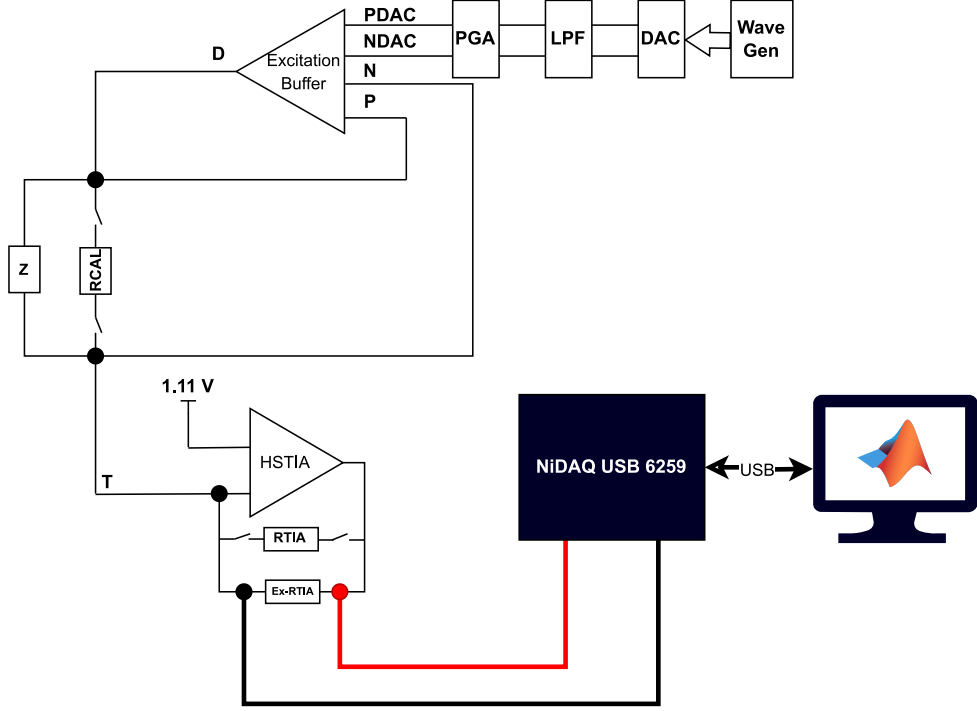


Figure 4.2: ADuCM355's impedance measurement system with external R_{TIA} . The voltage in that resistor is acquired with NiDAQ USB-6259 and processed in Matlab.

Signal processing consisted of using a low-pass filter with a cut-off frequency at 100 kHz and the subsequent DFT calculation. For the DFT, it was used a hamming window of 8192 points (DFT_{samp}) with an overlapping up to 90%. In this way, the final sampling frequency is computed using **Equation 4.4**:

$$F_s = \frac{ADC_{rate}}{DFT_{samp} * (1 - ovl/100)} \quad (4.4)$$

where ADC_{rate} is the NiDAQ sampling rate (500 kHz), and ovl is the overlapping in percentage. Therefore, using the overlapping of 90%, the maximum F_s reached is 610 Hz for the impedance signal.

4.3 Third method: SPI transmission to Raspberry and external processing.

The last method pretends to be a hybrid of the previous ones. The signal generation and acquisition are done with the ADuCM355, but the signal process is divided into two parts. The first is done internally to the ADuCM355 using the Sinc3 filter, while the second is done externally. In **Figure 4.3** is shown the overall connection between the ADuCM355, the Raspberry and an external computer.

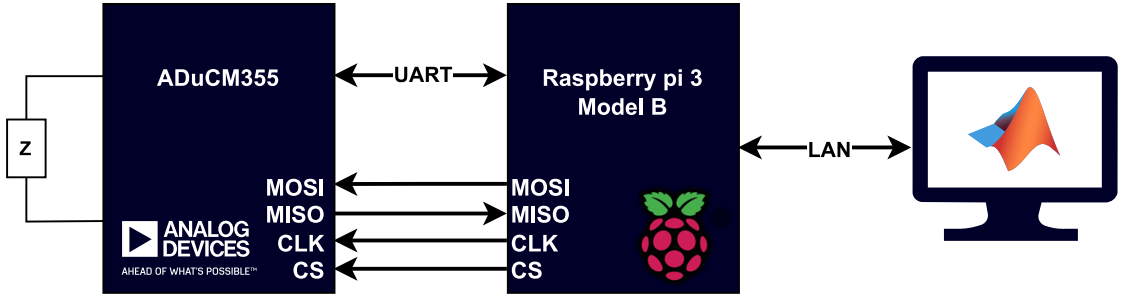


Figure 4.3: ADuCM355, Raspberry and computer connection for the third impedance measurement method.

UART and SPI were used to communicate the ADuCM355 with the Raspberry Pi 3. Via UART, the commands are sent from the Raspberry to control the ADuCM355, and the data captured by the ADuCM355's impedance measurement system is sent via SPI. This data was saved into the Raspberry to be sent by local areal network (LAN), and processed in an external computer.

The pipeline in Raspberry and the ADuCM355 must be synchronized, as shown in **Figure 4.4**, and follow these steps:

1. **Initialization:** The Raspberry and the ADuCM355 initialize the peripherals and all the other components for measurement and communication. The SPI was set to 6.4 MHz and the UART to 230,400 baud rate.
2. **Set R_{CAL} :** Raspberry sends the instruction to set the ADuCM355 for the R_{CAL} measurement via UART. At that moment, the ADuCM355 receives the UART interruption, verifies the instruction, and sets the R_{CAL} switches.
3. **R_{CAL} measurement:** At this point, the ADuCM355 starts the ADC reading, applies the Sinc3 filter, and finally stores them in the First Input First Output (FIFO) array.

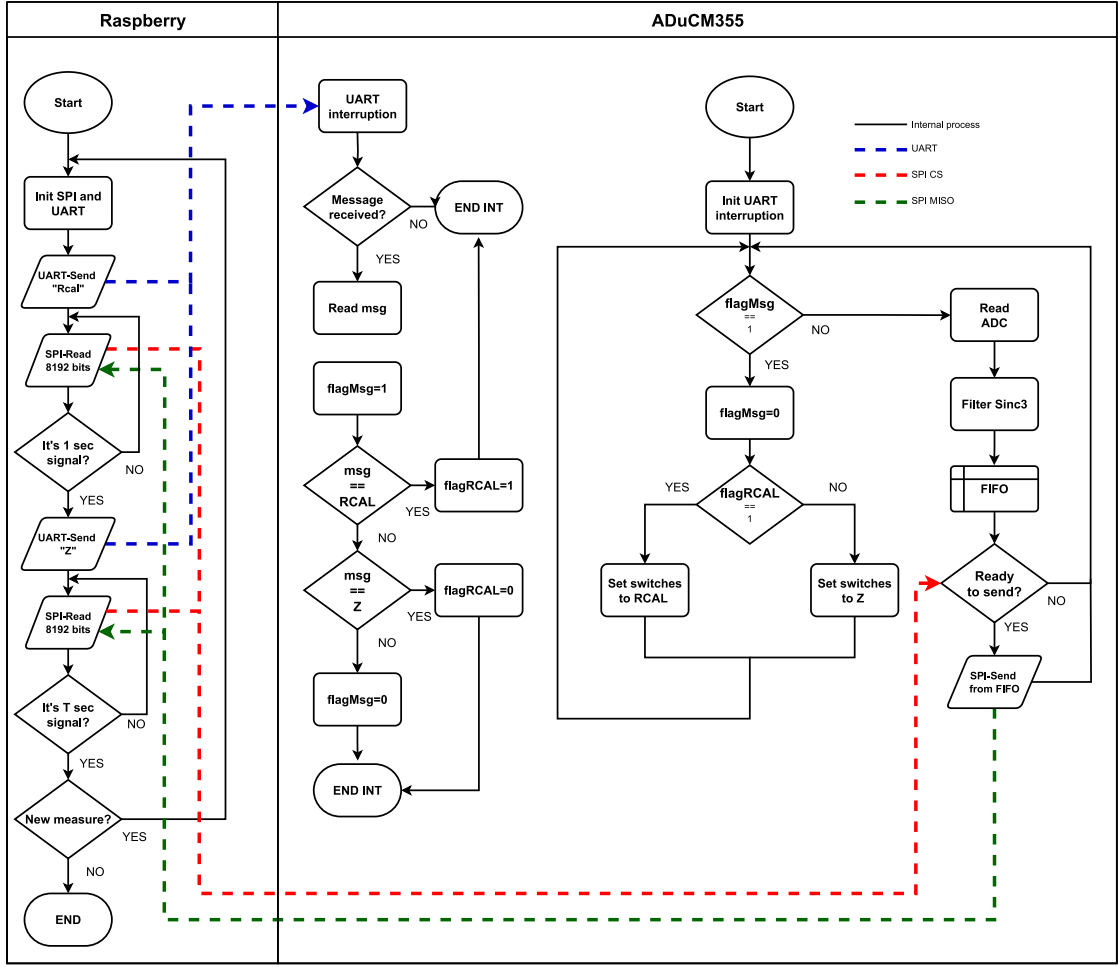


Figure 4.4: On the left Raspberry's pipeline and on the right the ADuCM355's pipeline. The blue line represents the UART communication. While red and green lines, stands for SPI communication. Red for the CS signal and the green line for MOSI signal

4. **Reading $RCAL$ data:** Raspberry uses a command to read the SPI data, which starts the communication, activating the CS. In that moment, the ADuCM355 sends the data saved into the FIFO via the MISO channel. Data is sent byte by byte, but the CS channel remains activated until 8192 bytes are sent, where each pair of bytes equals to one ADC data. The 8192 bytes were selected because, with these, it was possible to exploit all the ADuCM355 sampling rate.
5. **Acquisition time verification:** In this step, the acquisition time T was set. One second was set for the R_{CAL} case. If the time set had not elapsed

after step 4, step 4 is repeated.

6. **Configuring, measuring, and reading Z :** Finally, the steps from 2 to 5 are repeated, but configuring Z instead of R_{CAL} , and the acquisition time T was set depending on the test.
7. **Data storage:** R_{CAL} and Z data are stored in the Raspberry.

The stored data is sent to the external computer and processed. The signal process consisted of the DFT calculation, as done in the second method.

The final F_s reached was computed using **Equation 4.4**. For this method, the ADC_{rate} was 220 kHz and the F_s up to 268 Hz, which is lower than the obtained in second method, but it is better than the original sampling rate.

4.4 Validation Tests

The three designed tests were used to evaluate the capacity of the methods to measure the impedance. The following were the tests:

1. **Resistors measurement:** In this test were used between 10 and 15 resistors of different nominal values in the range $300\ \Omega$ - $3\ \text{k}\Omega$. Each resistor was measured for six seconds. This test evaluates the method's correctness to measure static resistance values. Also, the DFT's magnitude behavior was assessed for the second and third methods, because accessing that information for the first method was impossible.
2. **Potentiometer test:** A $10\ \text{k}\Omega$ potentiometer was used. This test evaluates the measurement behavior in a longer acquisition (60 sec), changing the potentiometer resistance from the lowest to the highest value. Each ten seconds the resistance value was increased and it was kept in the same value for the next ten second it had to be increased again.
3. **Respiration test:** This test was the first approach to the bioimpedance measurement. Two electrodes were placed on the sides of the subject trunk at the height of the chest as shown in **Figure 4.5**. The subject was a 25-year-old healthy adult male. The test duration was one minute, in which the subject did three deep breaths and normal breathing for the remaining time. This test aimed to see the feasibility of measuring the impedance in the body.

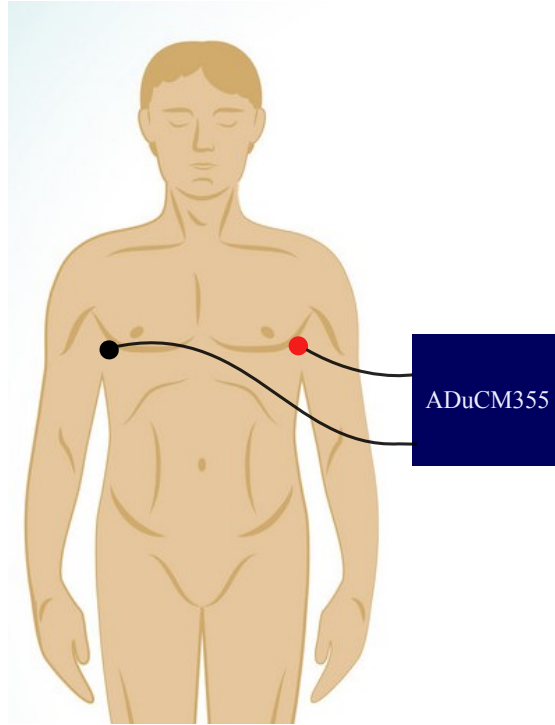


Figure 4.5: Respiration test configuration, two electrodes connected to the ADuCM355 placed on the sides of the trunk.

4.5 In vivo test: IPG signal acquisition

The in-vivo test was designed for the methods that passed the validation tests. It involves the ADuCM355 impedance acquisition and ECG measurement with the g.HIAMP, as a reference, to assess if the signal obtained is correlated with it. The complete setup can be seen in **Figure 4.6a**.

The carotid and radial arteries were the chosen to do the IPG acquisition. For each, two electrodes were placed at the skin over the artery in four different configurations: parallel (**Figure 4.6b**) and perpendicular (**Figure 4.6c**) to the artery axis with inter-electrode distances of 3 cm and 4 cm. The signal was recorded for one minute for each configuration.

The KendallTMH124SG electrodes from CardinalHealthTM used were used for the IPG acquisition. They were the smallest commercial electrodes found with a round shape of 30 mm x 24 mm size.

For the ECG, two electrodes were placed on the wrist, and the reference electrode was put on the left ankle. This signal recording started prior to the IPG acquisition.

However, when the last began, a trigger signal was activated in the ECG recording.

For comparison the ECG with the IPG signal, the last is realigned using as initial time the moment the trigger was activated in ECG. In addition, the Welch periodogram was calculated to analyze the components in frequency of the signal. It is essential to clarify that the comparison done in this test is qualitative because the two acquisition devices are not synchronized between them, and there was a delay between the ADuCM355 start and the the trigger activation.

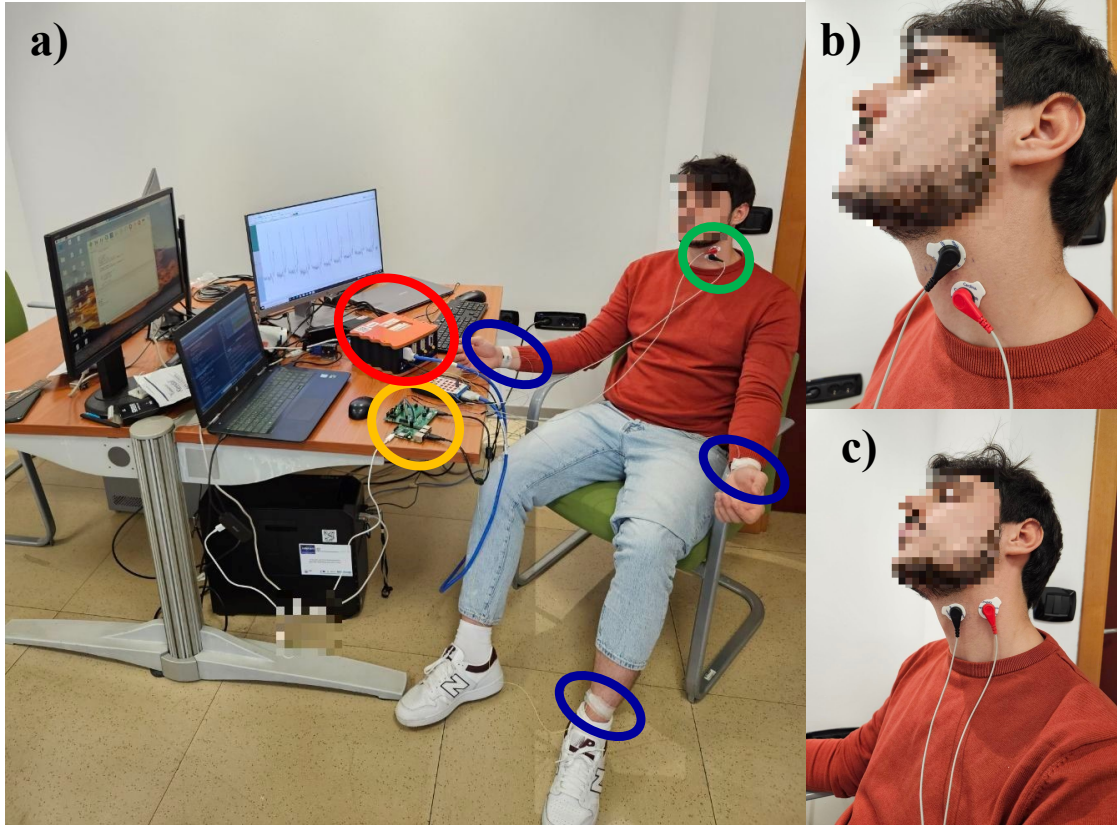


Figure 4.6: IPG acquisition setup. a) All the systems connected to the subject. The g.HIAMP is enclosed in red, the ECG electrodes are enclosed in blue, the ADuCM355 in yellow and the IPG electrodes in green. b) Parallel configuration of IPG electrodes. c) Perpendicular configuration of IPG electrodes

Chapter 5

Results

This section will be divided into four parts, each relative to the three validation test and the in-vivo test. The results will be discussed in each of them, and the suitability of the method is determined to continue with the subsequent test.

5.1 Resistors measurement

As described above, the first test consisted in measure various resistors of different values to check that the method used works correctly to acquire and compute the impedance. The measurements relative to the internal acquisition and processing of the ADuCM355 (First method) are shown in **Figure 5.1**.

It is essential to remember that this method was based on the Analog DevicesTM and then, as expected, shows a good performance that presents an average measurement error of $3.08\% \pm 2.16\%$. In addition, looking at **Figure 5.1**, it is observed that the measured Z finely approximates the expected linear behavior.

For the second method, which used the NiDaQ USB 6259 to acquire the signal and then process it externally, the measurement pipeline lets to get the DFT's magnitude, as shown in **Figure 5.2a**, and the Z computation, shown in **Figure 5.2b**.

Visually and numerically, this second method shows poor performance. It presents a very high mean error of $44.89\% \pm 28.96\%$. Furthermore, the DFT's magnitude does not clearly relate to the real Z value, which was expected to be inversely proportional. Evidently, if the DFT did not get the expected results, the computed Z values would not get them either.

From the third method, which combined the internal signal acquisition of the ADuCM355 from the first method with part of the external signal processing from

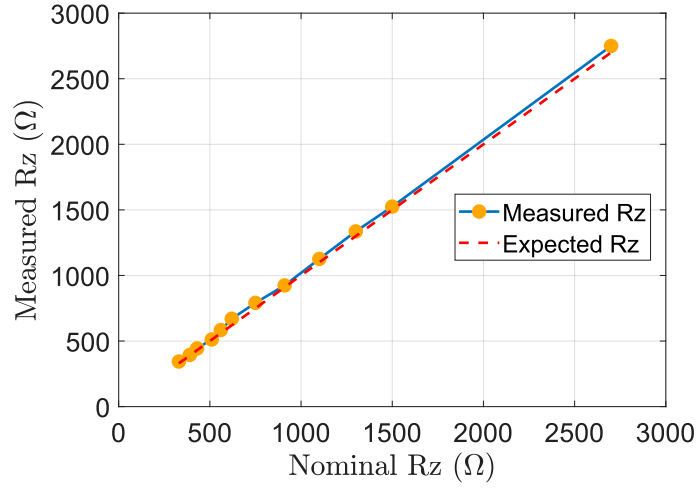


Figure 5.1: Results for resistors measurement for first method. It is compared the real resistor value with the measured.

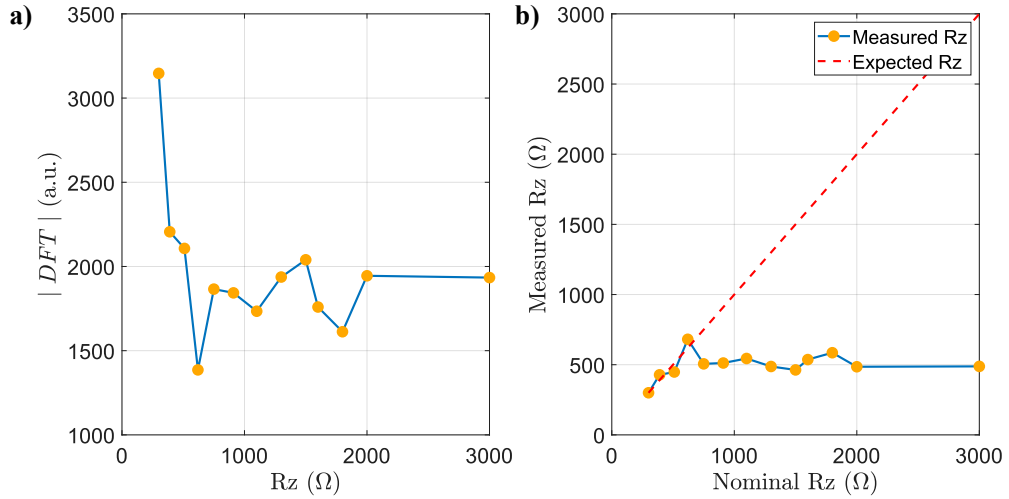


Figure 5.2: Second method results for resistors measurement. a) DFT's magnitude behavior, b) Comparison between real and measured resistance.

the second method, passing first by the SPI communication with the Raspberry, was possible to access to the DFT data, as shown in **Figure 5.3a**, and indeed to the measured impedances presented in **Figure 5.3b**.

Optically, this method meets the expectation for the DFT's behavior; it presents an approximately inversely proportional relation with the actual resistance, and

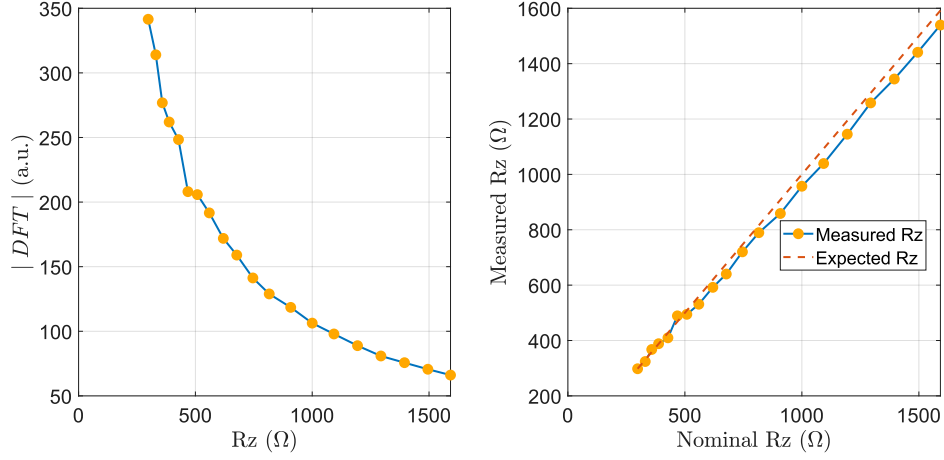


Figure 5.3: Third method results for resistors measurement. a) DFT's magnitude behavior, b) Comparison between real and measured resistance.

consequently, the calculated Z s show a linear behavior with a slight change in the line's slope, which is traduced in an average error of $3.49\% \pm 1.50\%$, which is very similar to the results obtained by the measurement base on the manufacture recommendations.

From those tests, it was decided to continue with the first and third methods, while the second method was discarded because the measurements were too far from the actual values.

That poor performance in the second method could be explained by how the acquisition was done with the NiDAQ. The NiDAQ introduces the equivalent to a parallel high-value resistance to R_{TIA} that could modify the current that passes through the last. If the current is modified, it is also the drop voltage, which is the one measured to compute the DFT.

5.2 Potentiometer test

The first and third methods were assessed with the potentiometer test because they successfully passed the resistors test. In this second test, the same potentiometer was used for the two methods. The internal ADuCM355 measurement method was tested first, and its results are shown in **Figure 5.4**.

The resistance values measured with this method are coherent with the nominal value of the potentiometer. In addition, the measurement followed a stepped shape, which was expected for how the test was designed. However, when the value should

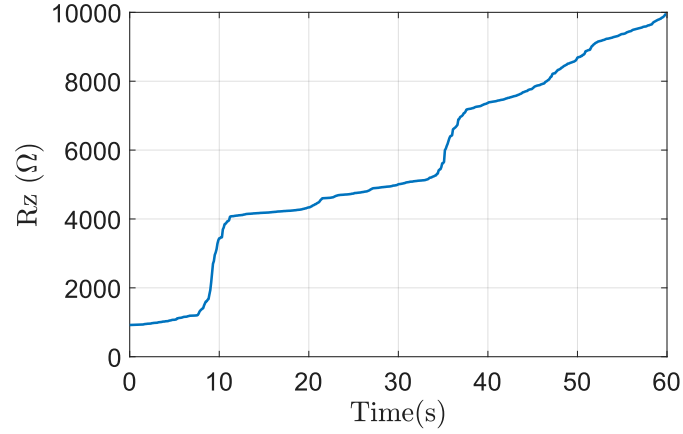


Figure 5.4: First method result for potentiometer test.

be constant, there is a slight increasing slope.

In contrast with the previous test, this one assessed all the recorded signal and not just the final average. So, it was the first time the third method would be assessed in that way, mainly because this measurement method involves data transmission that could be susceptible to loss of information. The signal recorded using the third method is presented in **Figure 5.5**.

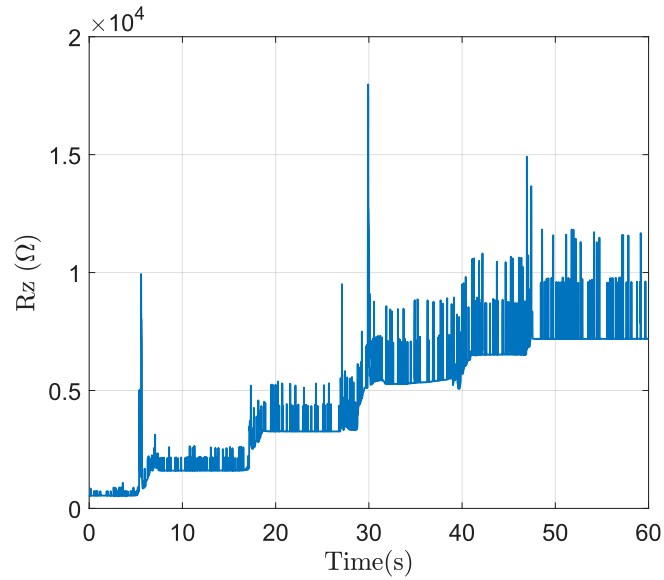


Figure 5.5: Signal recorded with the third method for the potentiometer test.

At first glance, it can be seen that the recorded signal with the third method is

full of undesirable peaks. Therefore, controlling DFT spectrum was done in two kinds of points. Where the signal with the expected value was the first type of point, its spectrum can be seen in **Figure 5.6a**. The other kind of points were those where the peaks were present, and their corresponding spectrum is shown in **Figure 5.6b**.

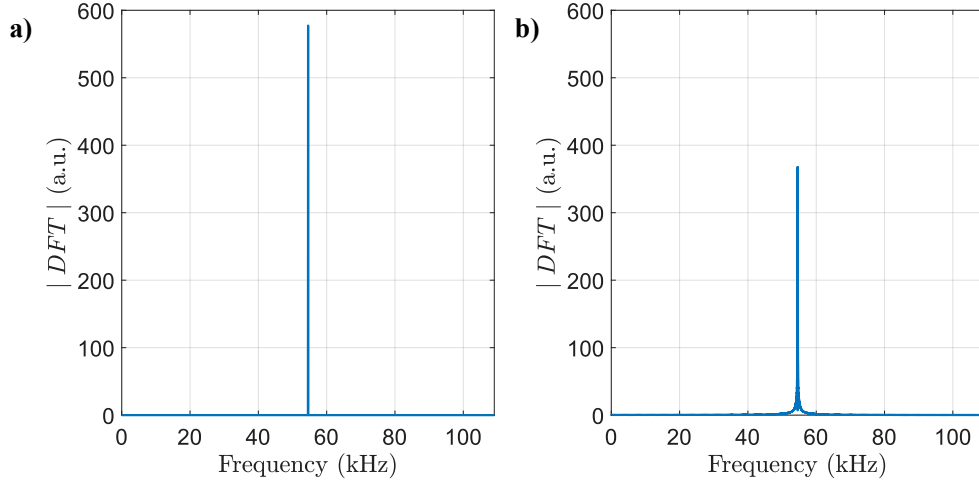


Figure 5.6: DFT spectrums for a) correct measurements and b) undesirable measures.

Comparing the spectrum of both kinds of points, the peak for the expected points is higher than the other peak. That is explained because, in the first one's spectrum, there is only the presence of one frequency, so the spectrum looks like just one line. In contrast, the spectrum looks more scattered for the undesirable points because there are minor components of other frequencies near the primary frequency. The signal in the time domain was analyzed, looking for the possible causes of that scattering, as shown in **Figure 5.7**.

The signal in the time domain presents a lack of data at some points, which causes a slight advance of the signal that generates the presence of other frequencies when calculating the DFT. The lack of information is likely due to data loss during SPI communication. However, it was impossible to find any periodicity or a particular pattern to determine the origin of it and any possible solution.

For the previous reason, it was decided to work with the impedance signal (**Figure 5.5**), which appears to show the expected behavior despite the undesirable peaks and correct the lack of data in post-processing. Therefore, a pipeline to eliminate these peaks and do an interpolation was designed.

The process of peak removal and interpolation consists of calculating the DFT

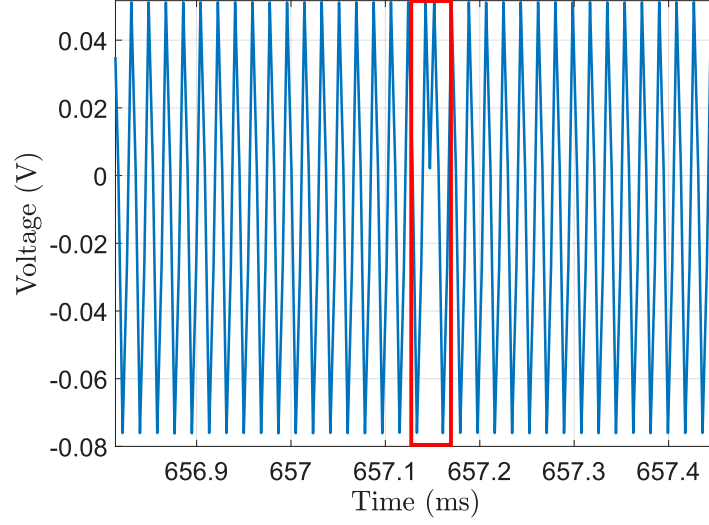


Figure 5.7: Acquired signal in time-domain before processing. Highlighted in the red box the lack of a data

as before and then computing the weight of the peak on the spectrum using **Equation 5.1**:

$$Weight_{F_p} = \frac{|DFT(F_p)|}{\sum_{f=0}^{F_{Ny}} |DFT(f)|} * 100 \quad (5.1)$$

where F_p is the primary frequency, and $|DFT(f)|$ is DFT's magnitude at the frequency f . If the weight of the peak is higher than a determined threshold (selected according to the signal), the point is accepted; if not, it is discarded. The process is repeated for all the signal, and a signal with some holes instead of peaks is obtained. The function *spline* of Matlab® was used to do a cubic interpolation to fill the holes.

The signal shown in **Figure 5.8** is obtained by applying the previous pipeline to the impedance signal acquired in the potentiometer test.

With the processed signal, the behavior for this test is more evident. The signal has shown a stepped shape as expected, and each step remains constant before it is increased, contrary to the drift present with the first measurement method. In addition, the resistance values are coherent with the potentiometer features. Although the processing cleaned a high percentage of the signal, some noise is still present.

After this test, both methods show a suitable performance. Each one has some

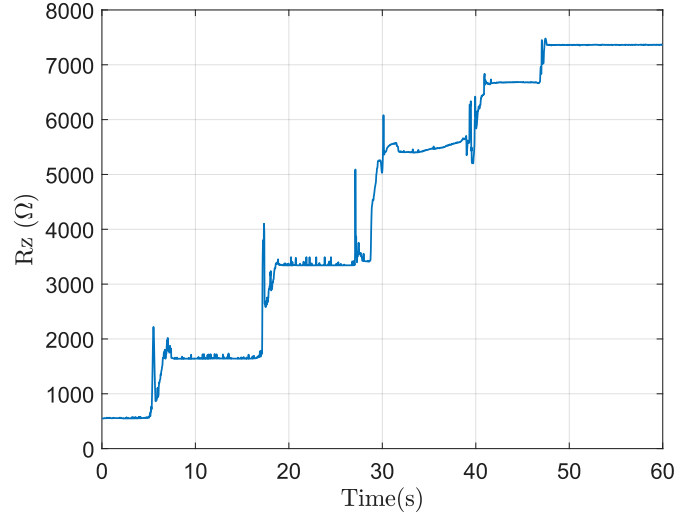


Figure 5.8: Third method signal for potentiometer test after peak removal and interpolation processing.

problems, but these are not significant enough to stop the measurement methods from following the next test.

5.3 Respiration test

In the respiration test is expected that the recorded signals the have first three peaks of high amplitude and long duration, relative to the three deep breaths done by the subject, and then other minor peaks but with a higher frequency, representing the normal subject's respiration. The first to be tested was the method that acquires and processes the signals inside the ADuCM355. The respiration signal obtained with the first method is shown in **Figure 5.9**.

As expected, the signal obtained has three high peaks, followed by regular breathing peaks. Normal respiration presents a maximum range (ΔZ) of 8Ω , which is in line with the literature that describes variations up to 5Ω [37]. In addition, the normal respiration frequency computed is approximately 13 breaths per minute, which is within the typical range for a healthy adult (12-20 breaths/min).

The third measurement method, which uses SPI communication to transmit the acquired data, was tested to obtain the respiration signal. The acquired impedance signal is seen in **Figure 5.10**.

As with the potentiometer test, the acquired signal is full of peaks, making it

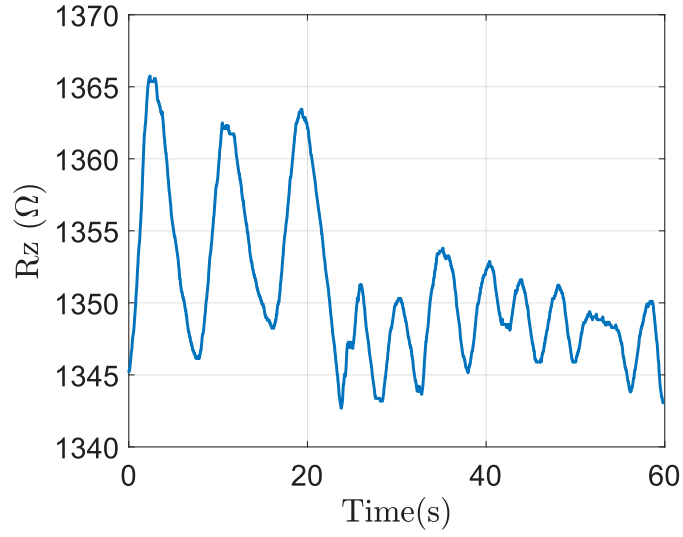


Figure 5.9: Respiration signal acquired with the internal ADuCM355 processing method.

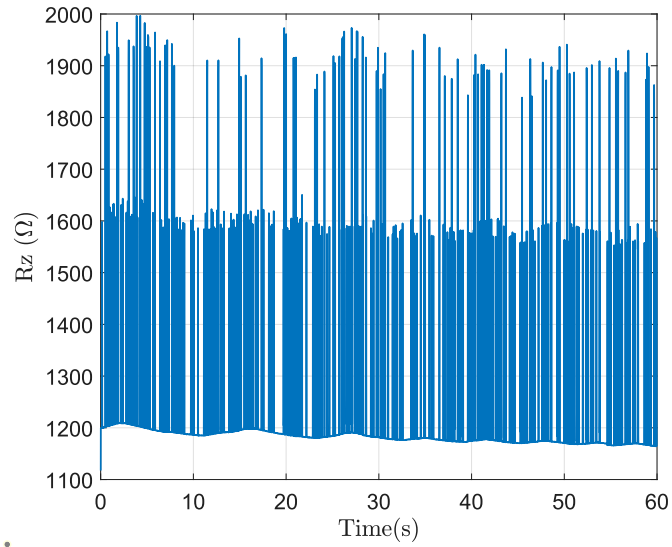


Figure 5.10: Third method signal for potentiometer test after peak removal and interpolation processing.

impossible to understand the signal pattern. So, as before, the peaks were removed, and the signal was interpolated to obtain the signals shown in **Figure 5.11**.

It is possible to appreciate better the expected peaks of the deep and normal

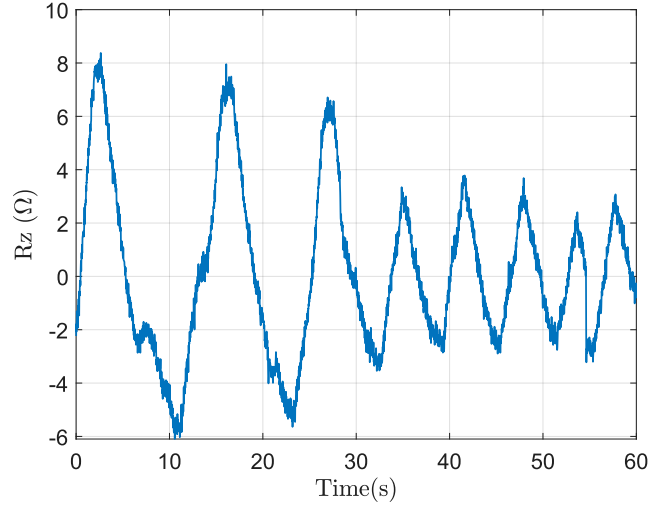


Figure 5.11: Third method signal for potentiometer test after peak removal and interpolation processing.

breaths with the cleaned signal. Also, the respiration frequency during normal breathing reaches 11 breaths per minute, and the variation in the impedance is lower than 7Ω . Therefore, the signal meets the expectations. However, it can be seen that the signal is more noisy than the one recorded with the first method.

This test was intended to assess the suitability of the measurement methods to acquire impedance signals from the human body, mainly because of the high resolution needed. In the bio-impedance signals the impedance variation is in the order of units of ohms and even thousandths of ohms. On the other hand, the resistors and potentiometer tests evaluated impedance changes in hundreds and thousands of ohms.

Both tested measurement methods reached the expected resolution, and the obtained pattern corresponds with the test design. In this way, these methods passed the three tests, and they were used to try to acquire the IPG signal, a signal that requires a higher resolution and has more frequency components.

5.4 Plethysmography acquisition test

For this last test, the two measurement methods that appeared suitable for acquiring the IPG to obtain the PW were assessed at the radial and carotid artery. Both methods were tested using the four electrode setups: Parallel-3 cm, Parallel-4 cm, Perpendicular-3 cm, and Perpendicular-4 cm.

The PW signal was tried to be first acquired at the radial artery. However, none of the methods acquired signals that showed similar behavior to what was expected in any electrode configurations.

The radial artery is very superficial to the skin, and its diameter is smaller than that of the carotid. The electric field generated by the electrodes probably goes too deep, causing a large volume of tissue to be captured, which makes the volume variation in the artery insignificant. It could be solved by decreasing the inter-electrode distance. However, the used electrodes do not allow to reduce it due to their size despite being the smallest commercial electrodes found.

The IPG at the carotid was the second artery assessed. Better results are expected because it is larger and deeper than the radial artery. Initially, with the measurement method that uses the Analog Devices™ recommendations, were acquired two typologies of signals. The first signal type was obtained in three of the four configurations, and an example of this signal and the ECG recorded with the g.HIAMP is shown in **Figure 5.12a-b**. In addition, an analysis of frequency was done using the Welch periodogram in order to determine which kind of biosignals or noise are present. The obtained frequency spectrum can be seen in **Figure 5.12c**.

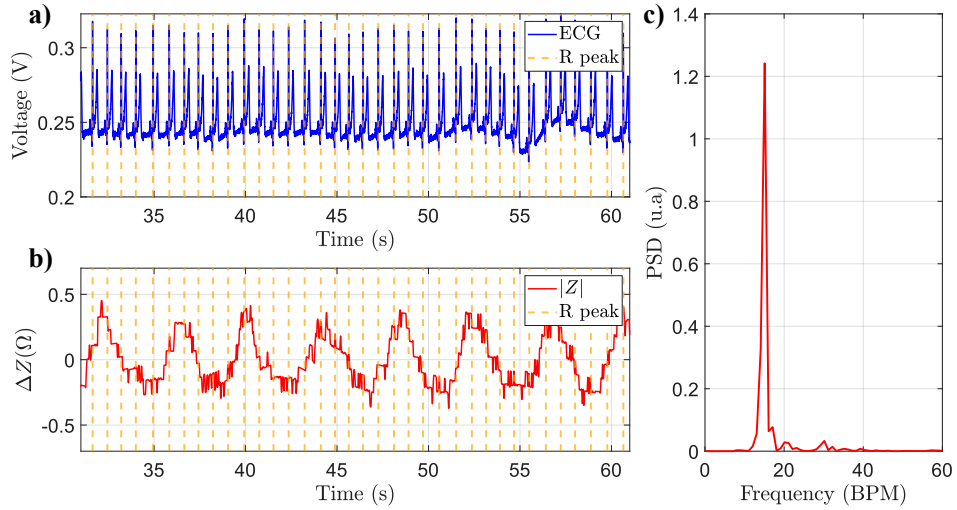


Figure 5.12: a)ECG signal, b)Impedance signal acquired with first measurement method c)Welch periodogram for the impedance signal.

In the acquired signal, a periodical pattern is observed. However, compared with the ECG, its periodicity is too long to be a PW signal. Regardless, another biological signal, such as respiration, could explain this behavior. The closeness of the carotid to the trachea and the primary frequency shown in the periodogram is approximately 0.25 Hz, equivalent to 15 breaths per minute, led to thinking that

the breathing causes this behavior. However, it was not verified with any reference device.

The signal was post-processed using a 0.5 Hz high-pass Butterworth filter to delete the respiration influence and a low-pass filter of 10 Hz to remove noise. The post-processed signal is shown in **Figure 5.13**.

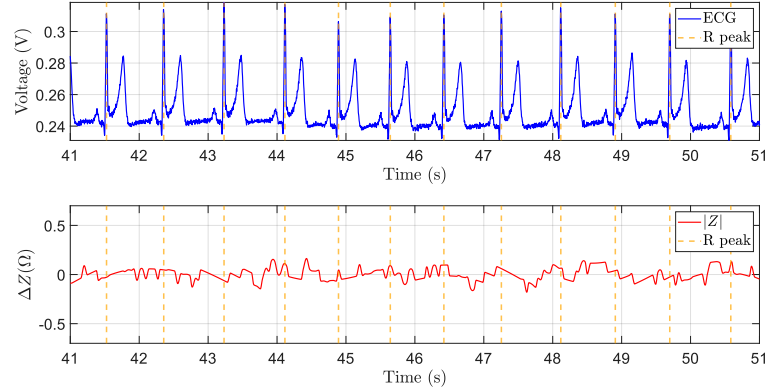


Figure 5.13: Filtered impedance signal(Red) compared with ECG signal (blue).

The obtained signal does not present any pattern similar to the expected PW. So, in this first type of acquired signals are just present the respiratory component but the plethysmographic is missing.

The second type of signal recorded with the first measurement method was obtained just with the electrodes placed perpendicular to the carotid axis with a distance between them of 4 cm. It was compared with the ECG, as shown in **Figure 5.14a-b**, and its frequency spectrum is in **Figure 5.14c**.

These signals also appear to have respiratory behavior with a frequency of 14 breaths per minute. The post-processing used was the same as for the previous signals. The filtered signal is shown in **Figure 5.15**.

A precise PW shape is absent in the filtered signal, but its regular behavior is comparable to the ECG periodicity. In addition, most of the waves have a peak, a slow decrement, and a sharp rise that could be relative to the systole ejection, diastole and systole beginning. However, it is impossible to state that the signal is a PW, mainly because the sampling frequency is not the most suitable for appreciating all the waveform components. For these reasons, the third measurement method seems appropriate for acquiring the IPG signal, due to its increased sampling frequency.

The third measurement method, which involves the data transmission between the ADuCM3 and the Raspberry Pi, was tested using the four identical setups for

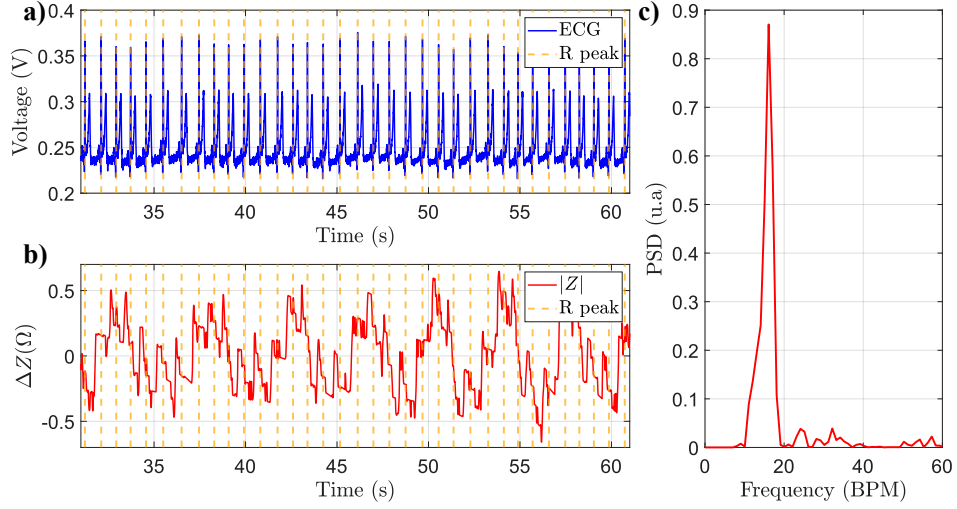


Figure 5.14: a) ECG signal, b) Impedance signal acquired with electrodes perpendicular to the carotid axis placed 4 cm between them, using the first measurement method, c) Welch periodogram for the impedance signal

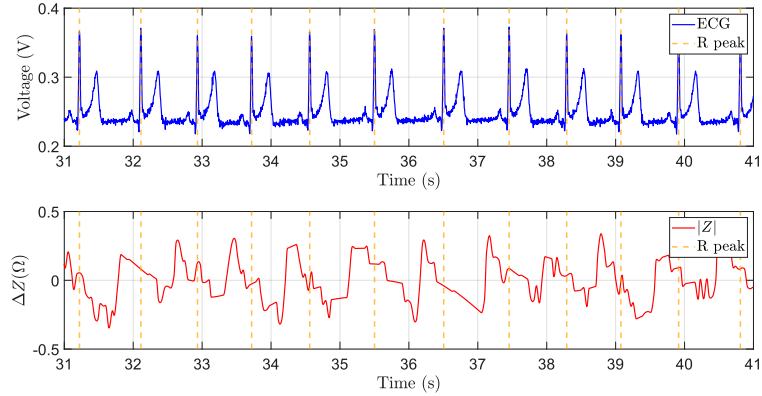


Figure 5.15: Filtered signal acquired in perpendicular-4 cm electrodes configuration (red), compared with the ECG (blue).

the electrodes. However, the result was the same for all configurations, as shown in **Figure 5.16a-b**. As before, a frequency analysis was done, and in **Figure 5.16b** is presented.

The breathing significantly impacts on this measurement technique, just as it did in the prior one, with a frequency of 12 breaths per minute is present throughout the recorded signal and for each electrodes setup. For these reasons, the high pass

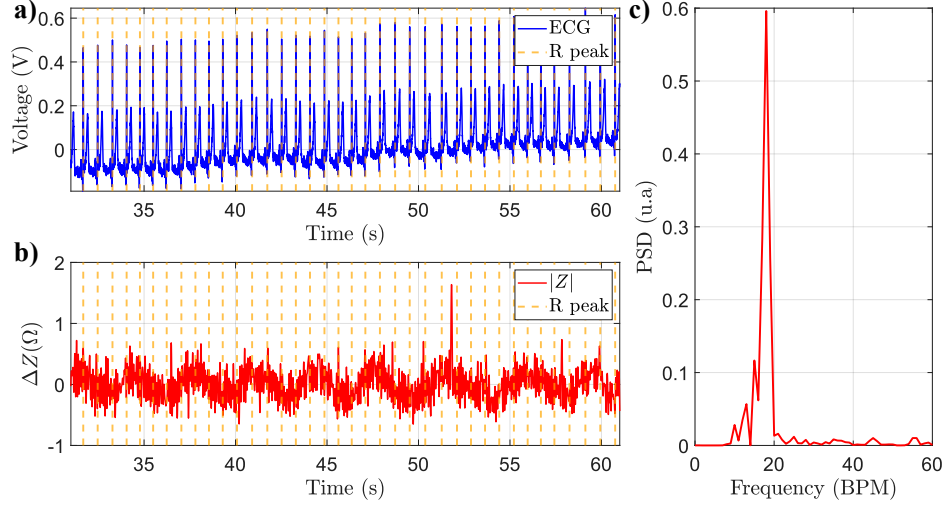


Figure 5.16: a) ECG signal, b) Impedance signal (red) acquired with third measurement method, c) Welch periodogram for the impedance signal

Butterworth filter of cut-off 0.5 Hz, and a low pass filter of 10 Hz were also applied. The filtered signal can be seen in **Figure 5.17**.

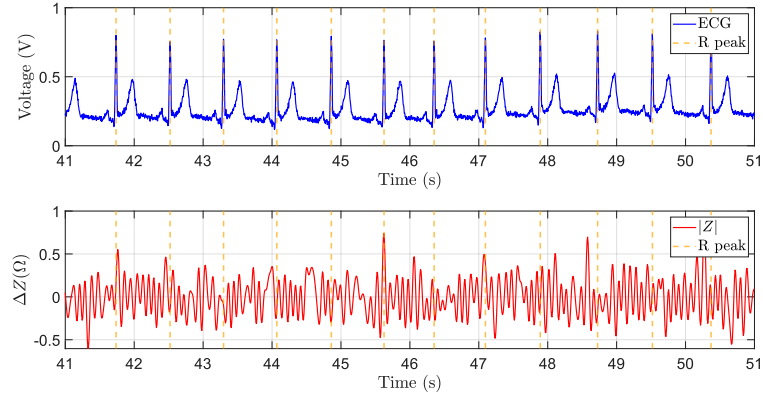


Figure 5.17: Filtered signal acquired in perpendicular-4 cm electrodes configuration (red), compared with the ECG (blue).

The filtered signal does not show any particular pattern similar to the expected PW. This behavior is not strange because it happened before in three of the four electrode configurations used with the first measurement method, in which the impedance average value acquired went from 1 k Ω to 1.5 k Ω , which was within the expected value for the body impedance that should be around 1 k Ω [30]. Even

though the method, in combination with the electrode setup, does not capture the ΔZ for PW signal with enough resolution, that should be lower than $1\ \Omega$ [30],[31].

For the three electrodes configuration, Perpendicular-3 cm, Parallel-3 cm and Parallel-4 cm, it can be assumed that the electrodes placement does not allow the impedance changes to be captured effectively. In the parallel setup, it is possible that by taking a larger artery region, a higher blood volume is considered, and the variation in the volume due to blood flow is less significant. Meanwhile, a smaller volume is taken in perpendicular positioning, which implies being more sensitive when it changes. Nonetheless, for the perpendicular configuration, it is also essential that the inter-electrode distance let the signal go deep enough to reach the carotid; then, with 3 cm, it was not possible to arrive at the artery.

It was possible to acquire what appears to be a PW signal using just the internal components and processing of the ADuCM355 and using the Perpendicular-4 cm electrodes setup. However, for the same configuration, the third method did not reach to acquire the expected signal even with a higher sampling frequency.

Perhaps the most notorious problem is losing information during SPI data transmission. Removing the peaks and interpolating the signal seemed enough to solve this downside. Indeed, that processing allows the analysis of signals with impedance variation around $5\ \Omega$, as the respiration, but for lower changes in the impedance, the interpolation makes assumptions that are more significant on that scale, affecting more the actual signal to be analyzed.

The ADuCM355 was used as slave during the communication with the Raspberry Pi 3, then, the control of the communication rested on the last one. Thus, it may have happened that Raspberry requested the ADuCM355 to send the data when it was not ready yet. The most obvious solutions for this problem are to use the ADuCM355 as master or implement a better communication protocol. For the first case, changing the Raspberry to another device is required because it can work only as a Master in SPI. In the second case, implementing a more robust communication protocol was proved. However, the amount of data required to transmit was so high that adding more instructions and steps during the acquisition and communication caused the ADuCM355 to take longer to process the data before sending it, so the missing information increased.

The signal processing could be another difficulty presented in the third measurement method because for the signal demodulation, was used DFT, which is sensitive to undesirable frequencies, as seen in the obtained signals. The DFT was chosen to try to emulate the Analog DevicesTM process but overlapping the window to increase the final sampling rate. However, it is unclear how the ADuCM355 calculates the DFT's magnitude and how it manages the influence of other frequencies. Thus, it is necessary to delve into how to deal with the noise in the DFT spectrum or

even look for different demodulation techniques that are not too sensitive to small changes in frequency.

The electrode positioning and setup may also have affected the measurement repeatability because the carotid is surrounded by a thick layer of tissue, which makes the changes in impedance more imperceptible, and it is close to other organs, such as the trachea, which adds noise, as the breathing, and motion artifacts by swallowing. Therefore, a precise placement of the electrodes could be required to acquire the expected data. The numerosity of tests needs to be increased to determine the most suitable configuration to acquire the PW signal.

Chapter 6

Conclusions

Arterial stiffness is an essential indicator to detect and prevent the CVDs. The PWV is the gold standard to measure this condition, that is commonly computed using the applanation tonometry. However, this technique presents some difficulties related to operator dependence and the impossibility of being used for continuous monitoring.

The IPG emerged as an interesting and novel measurement principle to detect the PW because it relates changes in impedance with the volume variation. For this reason, the microcontroller ADuCM355, designed with an internal impedance measurement system, was chosen.

The ADuCM355 generated and injected a fixed tension to the Z load of interest. However, three methodologies were assessed for the current measurement and signal processing: ADuCM355's internal acquisition and processing, external acquisition using the NiDAQ-USB6259 and MATLAB processing, and internal acquisition and external processing.

The second method was the one with the poorest performance. The most probable cause is a leaking current during the measurement. Therefore, studying other possible of acquiring the signal should be recommended, such as adding a voltage follower after the TIA.

For the other two methods, there was an acceptable behavior for measuring static and variable resistances in the hundreds and thousands of ohms range. Using only the ADuCM355's components and the suggested pipeline by the manufacturer to compute the impedance is unsuitable for acquiring the IPG signal. Even though one electrode configuration seems to capture the PW, the low sampling rate does not allow it to be stated. On the other hand, the combination of the ADuCM355 acquisition and external processing that raises F_s has various inter-medial steps,

such as the SPI transmission, elevating the error probability. However, both methods are suitable enough to record other bio-signals, such as respiration, which has lower frequency components and requires a lower impedance resolution.

For further studies, it is recommended to increment the number of in-silico and in-vivo tests to determine the best arteries and electrode configurations to acquire the IPG signal. Try different types and sizes of electrodes is also advisable.

Relative to the signal acquisition and processing, if the ADuCM355 is continued, at least the processing must be external to the microcontroller to increment the sampling rate. Therefore, the SPI protocol communication must be improved, or the ADuCM355 should perform as Master, so a device to replace the Raspberry Pi should be searched. However, investigating other possible micro-controllers to measure impedance or design a custom circuit could be considered.

Bibliography

- [1] National Heart Lung, Blood InstituteNational Heart Lung, and Blood Institute. *Causes and risk factors*. URL: <https://www.nhlbi.nih.gov/health/heart-attack/causes> (cit. on p. 1).
- [2] N M van Popele et al. «Association between arterial stiffness and atherosclerosis: the Rotterdam Study». en. In: *Stroke* 32.2 (Feb. 2001), pp. 454–460 (cit. on p. 1).
- [3] Patrick Segers, Ernst R. Rietzschel, and Julio A. Chirinos. «How to Measure Arterial Stiffness in Humans». In: *Arteriosclerosis, Thrombosis, and Vascular Biology* 40.5 (2020), pp. 1034–1043. DOI: 10.1161/ATVBAHA.119.313132. URL: <https://www.ahajournals.org/doi/abs/10.1161/ATVBAHA.119.313132> (cit. on pp. 1, 17, 18).
- [4] Tânia Pereira, Carlos Correia, and João Cardoso. «Novel methods for pulse wave velocity measurement». en. In: *J. Med. Biol. Eng.* 35.5 (Oct. 2015), pp. 555–565 (cit. on pp. 1, 2, 14, 16, 18–20).
- [5] N. De Pinho Ferreira, C. Gehin, and B. Massot. «A Review of Methods for Non-Invasive Heart Rate Measurement on Wrist». In: *IRBM* 42.1 (2021), pp. 4–18. ISSN: 1959-0318. DOI: <https://doi.org/10.1016/j.irbm.2020.04.001>. URL: <https://www.sciencedirect.com/science/article/pii/S1959031820300804> (cit. on pp. 2, 22).
- [6] David E. Mohrman and Lois Jane Heller. «Overview of the Cardiovascular System». In: *Cardiovascular Physiology, 9e*. New York, NY: McGraw-Hill Education, 2018. URL: accessmedicine.mhmedical.com/content.aspx?aid=1153946098 (cit. on pp. 3–5, 10–12).
- [7] K.E. Barrett, S.M. Barman, S. Boitano, and H. Brooks. *Ganong's Review of Medical Physiology, 24th Edition*. LANGE Basic Science. Mcgraw-hill, 2012. ISBN: 9780071780032 (cit. on pp. 3, 6–8, 11, 12, 15).

- [8] L.S. Lilly and Harvard Medical School. *Pathophysiology of Heart Disease: A Collaborative Project of Medical Students and Faculty*. Online access: Lippincott LWW Health Library: Integrated Basic Sciences Collection. Wolters Kluwer, 2016. ISBN: 9781451192759 (cit. on pp. 5, 6).
- [9] Jonathan D. Kibble. «The Cardiovascular System». In: *The Big Picture Physiology: Medical Course & Step 1 Review, 2e*. New York, NY: McGraw Hill, 2020. URL: accessmedicine.mhmedical.com/content.aspx?aid=1172666984 (cit. on p. 5).
- [10] J.E. Hall and M.E. Hall. *Guyton and Hall Textbook of Medical Physiology E-Book: Guyton and Hall Textbook of Medical Physiology E-Book*. Guyton Physiology. Elsevier Health Sciences, 2020. ISBN: 9780323640039 (cit. on pp. 6–9, 12–15).
- [11] Franklin H. Zimmerman. «From Electrophysiology to Electrocardiography». In: *ECG Core Curriculum*. New York, NY: McGraw Hill Education, 2023. URL: accessmedicine.mhmedical.com/content.aspx?aid=1200099827 (cit. on pp. 9, 10).
- [12] Klaas Rinse Visser. «Electric properties of blood and impedance cardiography». English. date_{submitted} : 2008 Rights : University of Groningen. PhD thesis. University of Groningen, 1992 (cit. on p. 13).
- [13] A L Zuev, N N Shakirov, A I Sudakov, and V Ju Mishlanov. «Pulse Related Changes in Electrical Impedance of Blood Vessels: Physical, Experimental and Modelling Aspects». In: *Journal of Physics: Conference Series* 1945.1 (June 2021), p. 012065. DOI: 10.1088/1742-6596/1945/1/012065. URL: <https://dx.doi.org/10.1088/1742-6596/1945/1/012065> (cit. on p. 13).
- [14] Adam Timmis et al. «European Society of Cardiology: Cardiovascular disease statistics 2019». en. In: *Eur. Heart J.* 41.1 (Jan. 2020), pp. 12–85 (cit. on p. 13).
- [15] Edgardo Olvera Lopez, Briand D. Ballard, and Arif Jan. «Cardiovascular Disease». In: *National Library of Medicine* (Aug. 2023). URL: <https://www.ncbi.nlm.nih.gov/books/NBK535419/> (cit. on p. 13).
- [16] A J Lusis. «Atherosclerosis». en. In: *Nature* 407.6801 (Sept. 2000), pp. 233–241 (cit. on p. 13).
- [17] Alberto Avolio. «Arterial stiffness». en. In: *Pulse (Basel)* 1.1 (Apr. 2013), pp. 14–28 (cit. on p. 14).

- [18] Stephen A. Esper and Michael R. Pinsky. «Arterial waveform analysis». In: *Best Practice Research Clinical Anaesthesiology* 28.4 (2014). Hemodynamic Monitoring Devices, pp. 363–380. ISSN: 1521-6896. DOI: <https://doi.org/10.1016/j.bpa.2014.08.002>. URL: <https://www.sciencedirect.com/science/article/pii/S1521689614000718> (cit. on p. 15).
- [19] Registered Nurse RN. *Pulse Points Nursing Assessment*. May 2019. URL: <https://www.registerednursen.com/pulse-points-nursing-assessment/> (cit. on p. 16).
- [20] PulsePen®. *Arterial tonometry*. URL: <https://pulsepen-me.com/arterial-tonometry/> (cit. on pp. 17, 19).
- [21] Toan Huu Huynh, Roozbeh Jafari, and Wan-Young Chung. «Noninvasive Cuffless Blood Pressure Estimation Using Pulse Transit Time and Impedance Plethysmography». In: *IEEE Transactions on Biomedical Engineering* 66.4 (2019), pp. 967–976. DOI: 10.1109/TBME.2018.2865751 (cit. on pp. 18, 21, 22).
- [22] Andrew L Wentland, Thomas M Grist, and Oliver Wieben. «Review of MRI-based measurements of pulse wave velocity: a biomarker of arterial stiffness». en. In: *Cardiovasc. Diagn. Ther.* 4.2 (Apr. 2014), pp. 193–206 (cit. on pp. 18, 19, 34).
- [23] Jordi Calabia, Pere Torguet, Maria Garcia, Isabel Garcia, Nadia Martin, Bernat Guasch, Diana Faur, and Martí Vallés. «Doppler ultrasound in the measurement of pulse wave velocity: agreement with the Complior method». In: *Cardiovascular Ultrasound* 9.1 (Apr. 2011), p. 13 (cit. on pp. 18, 19).
- [24] Sphygmocor®XCEL. *Operator’s manual SphygmoCor XCEL System v1*. 13th. Available at https://atcormedical.com/wp-content/uploads/simple-file-list/Downloads/SphygmoCor-XCEL-V1_3-Operators-Manual.pdf. Sphygmocor®. Sideney, AU, 2022 (cit. on p. 19).
- [25] Tensiomed. *Aortic Pulse Wave Velocity (PWVao)*. URL: <https://www.tensiomed.com/parameters/aortic-pulse-wave-velocity-pwvao/> (cit. on p. 20).
- [26] Irene Buraioli, Davide Lena, Alessandro Sanginario, Dario Leone, Giulia Mingrone, Alberto Milan, and Danilo Demarchi. «A New Noninvasive System for Clinical Pulse Wave Velocity Assessment: The Athos Device». In: *IEEE Transactions on Biomedical Circuits and Systems* 15.1 (2021), pp. 133–142. DOI: 10.1109/TBCAS.2021.3058010 (cit. on p. 20).

- [27] Jan M. Sloves, Jose I. Almeida, Priscila Gisselle Sanchez Aguirre, and Andrew M. Abi-Chaker. «Chapter 4 - Venous Diagnostic Tools». In: *Atlas of Endovascular Venous Surgery (Second Edition)*. Ed. by Jose I. Almeida. Second Edition. Philadelphia: Elsevier, 2019, pp. 63–119. ISBN: 978-0-323-51139-1. DOI: <https://doi.org/10.1016/B978-0-323-51139-1.00004-8>. URL: <https://www.sciencedirect.com/science/article/pii/B9780323511391000048> (cit. on p. 21).
- [28] Malcolm J. Dennis. «Plethysmography: the new wave in haemodynamic monitoring – a review of clinical applications». In: *Australian Critical Care* 13.1 (2000), pp. 14–20. ISSN: 1036-7314. DOI: [https://doi.org/10.1016/S1036-7314\(00\)70611-4](https://doi.org/10.1016/S1036-7314(00)70611-4). URL: <https://www.sciencedirect.com/science/article/pii/S1036731400706114> (cit. on p. 21).
- [29] John Allen. «Photoplethysmography and its application in clinical physiological measurement». en. In: *Physiol. Meas.* 28.3 (Mar. 2007), R1–39 (cit. on p. 21).
- [30] Jianman He, Mengjun Wang, Xiaoxia Li, Gang Li, and Ling Lin. «Pulse wave detection method based on the bio-impedance of the wrist». In: *Review of Scientific Instruments* 87.5 (May 2016), p. 055001. ISSN: 0034-6748. DOI: [10.1063/1.4947514](https://doi.org/10.1063/1.4947514). URL: <https://doi.org/10.1063/1.4947514> (cit. on pp. 22, 32, 33, 35, 54, 55).
- [31] A. I. P. Wiegerinck, A. Thomsen, J. Hisdal, H. Kalvøy, and C. Tronstad. «Electrical impedance plethysmography versus tonometry to measure the pulse wave velocity in peripheral arteries in young healthy volunteers: a pilot study». In: *Journal of Electrical Bioimpedance* 12.1 (2021), pp. 169–177. DOI: [doi:10.2478/joeb-2021-0020](https://doi.org/10.2478/joeb-2021-0020). URL: <https://doi.org/10.2478/joeb-2021-0020> (cit. on pp. 23, 32, 35, 55).
- [32] Kwonjoon Lee and Hoi-Jun Yoo. «Simultaneous Electrical Bio-Impedance Plethysmography at Different Body Parts: Continuous and Non-Invasive Monitoring of Pulse Wave Velocity». In: *IEEE Transactions on Biomedical Circuits and Systems* 15.5 (2021), pp. 1027–1038. DOI: [10.1109/TBCAS.2021.3115021](https://doi.org/10.1109/TBCAS.2021.3115021) (cit. on pp. 23, 32).
- [33] *ADuCM355 Hardware Reference Manual*. UG-1262. Rev. B. Analog Devices. 2019 (cit. on p. 24).
- [34] RaspberryPi. *Raspberry pi documentation*. URL: <https://www.raspberrypi.com/documentation/> (cit. on p. 29).
- [35] *PCI/PCIe/PXI/PXIe/ USB-625 Specifications*. National Instruments. 2023 (cit. on p. 29).
- [36] *g.Hiamp-Research instruction for use*. V1.16.01. Guger Technologies. 2017 (cit. on p. 30).

- [37] C. Redmond. *Transthoracic Impedance Measurements in Patient Monitoring*. Tech. rep. MS-2458. Norwood, MA 02062-9106, U.S.A: Analog Devices, 2013, p. 5. URL: <https://www.analog.com/en/technical-articles/transthoracic-impedance-measurements-in-patient-monitoring.html> (cit. on p. 48).